POLITECNICO DI TORINO

MASTER's Degree in ELECTRICAL ENGINEERING

MASTER's Degree Thesis

Design of magnetic gears for aerospace applications

Supervisors
Prof. MAURIZIO REPETTO
Prof. CARLO ROSSO

Candidate
SALVATORE FAZIO

22 March 2021

Summary

This document contains some studies for the coaxial magnetic gearbox in the Aerospace domain. The analysis proposes several Finite Element Models (FEM) to compute the static torque characteristic and the torque density.

The first FEM model implements the classical Coaxial Magnetic Gear (CMG) model characterised by p_{in} pair of poles in the internal part and p_{out} pair of poles in the external part. The first step was characterised considering linear iron. Once the model was validated, a comparison with two Fe-Si Alloys was done and results obtained show congruence in terms of useful torque and volumetric torque.

Also the Halbach permanent magnet arrangement was used to find a valid strategy to decrease the CMG mass. Without the internal and the external yoke, torque performances are lower because fewer flux lines cross the iron modulator. Adding the two iron yokes low the torque returns on the same order rather than the traditional CMG with an imposed external radius.

Acknowledgements

I want to thank all the people I have met throughout my university career. First of all, I would like to thank the entire Electrical Engineering staff, in the person of Prof. Aldo Canova and Prof. Freschi, which during the generalised lockdown of the pandemic did good support to all Erasmus students.

My heartfelt thanks also go to my two lecturers, Prof. Repetto and Prof. Rosso, who, in the midst of a thousand commitments, gave me the support I needed to complete my thesis.

Finally, I would like to dedicate this achievement to my family who, in sad and dark moments, continued to spur me giving the best in every situation.

Table of Contents

List of Tables

List of Figures

Acronyms

CMG

Coaxial Magnetic Gearbox

HP

Hydraulic Pump

IDG

Integrated Drive Generator

OPU

Oil Pump Unit

PM

Permanent Magnet

Chapter 1

Introduction

Nowadays, electrical and magnetic components, in the aerospace and automotive domain, tend to replace mechanical parts over time. This work aims to understand the Magnetic Gearbox (MG) performances compared with a traditional mechanical gear. It is useful to consider this system as an interface between transmission chains, which works having different angular speeds.

In particular, magnetic gearboxes need reduced maintenance, produce minimum noise and work also in overload conditions. The disadvantages, instead, are a larger size and a higher cost, mainly concerning the permanent magnet material, in the inner and outer rotor.

As the use of MG is relatively new, as a first approach, to understand coaxial MG's general advantages and drawback, a detailed research has been carried out by analysing scientific literature.

The analysis is focused on the aircraft accessories architecture where the MG act as a constant angular speed reducer. The CMG study uses in this context a planar Finite Element Model (FEM). In particular, the two dimensional FEMM code has been used.

Initially, the FEMM models developed has used ferromagnetic linear materials. After that, to have a realistic evaluation, the analysis has been focused on non-linear ferromagnetic materials. Concerning the traditional CMG, the evaluation gives indications about torque performances and masses. Finally, the Halbach array structure was implemented to understand differences in terms of useful torque.

The main industrial contexts are aerospace and automotive propulsion systems. For aerospace, there are some linkings concerning the auxiliary propulsion systems (e.g. accessory units) and the propeller drive. In the automotive domain, instead, MGs replace mechanical gearboxes with different transmission ratios for both internal combustion and electric propulsion motors.

Chapter 2

State of the art

The development of MG technology begins in 1916, with a simple power transmission between two aligned shafts by means of a magnetic coupling. A few years later, Chubb (1933) proposed an improvement where a Vernier motor was used as a magnetic reduction-gear unit [1]. In the early 1940s, the innovation of Aluminium-Nickel-Cobalt (AlNiCo) PMs didn't lead to high performances. However, the first complete Magnetic Gearbox system was proposed by Martin Jr. (1968). It consists of three rotary cylinders with different types of PMs. As an improvement, in 1972, Laing introduced an optimized version with a plurality of magnetic poles in two PM pole rings.

At the beginning of the 1980s, with the development of high-performance PMs (NdFeB permanent magnets), different MG (magnetic gearbox) typologies didn't present high performances because of the low Torque density.
However, parallel developments were conducted for electrical power generation applications, where high and low-speed rotors are coupled through several stationary steel segments [2]. An example is in the reference [3], where surface-mounted magnets in the high-speed were replaced with interior-spoke magnets. This gearbox has high torque density and the same velocity ratio.

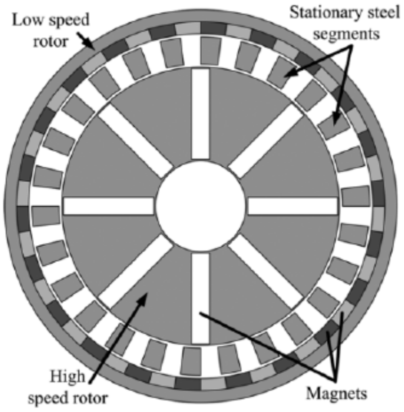

Figure 2.1: MG with interior-spoke magnets(document planetary MG)[4]

Later, Okano et al. [5] created a superconducting MG versions . The combination between super-conduction and magnets improved the transmission torque capacity. But all the improvements added some disadvantages, like the considerable volume due to the required cooling system and the power source. [4] However, the most consolidated technologies used in an industrial context are the harmonic, planetary and the coaxial MG

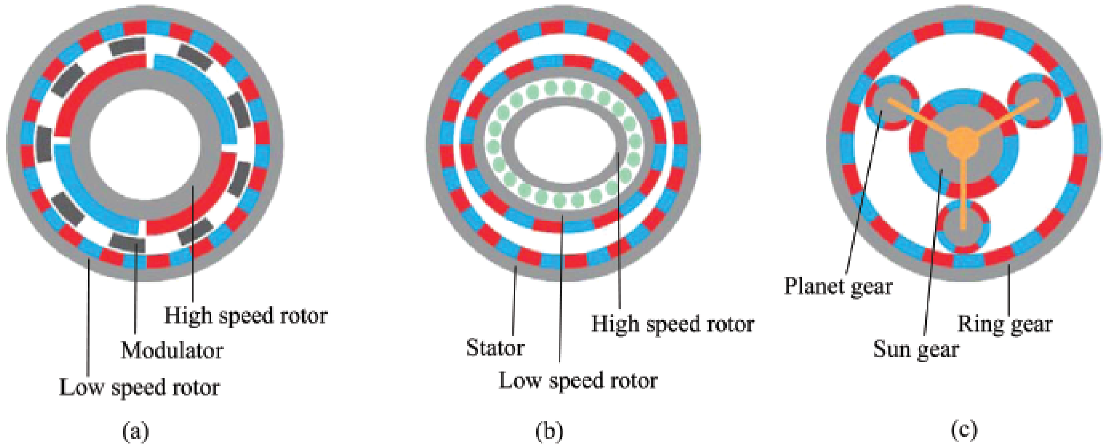

Figure 2.2: Coaxial (a), Harmonic (b) and planetary (c) MG [1]

2.1 Harmonic magnetic gearbox

The harmonic MG has his application for a waveform generator. The base structure from the external to the internal part is composed by:

- an eccentric low speed rotor with p_out pair of poles.
- an eccentric high speed rotor that acts like an equivalent wave generator for the traditional mechanical gear
- a stator defined with $p_s = p_r + 1$ pair of poles.

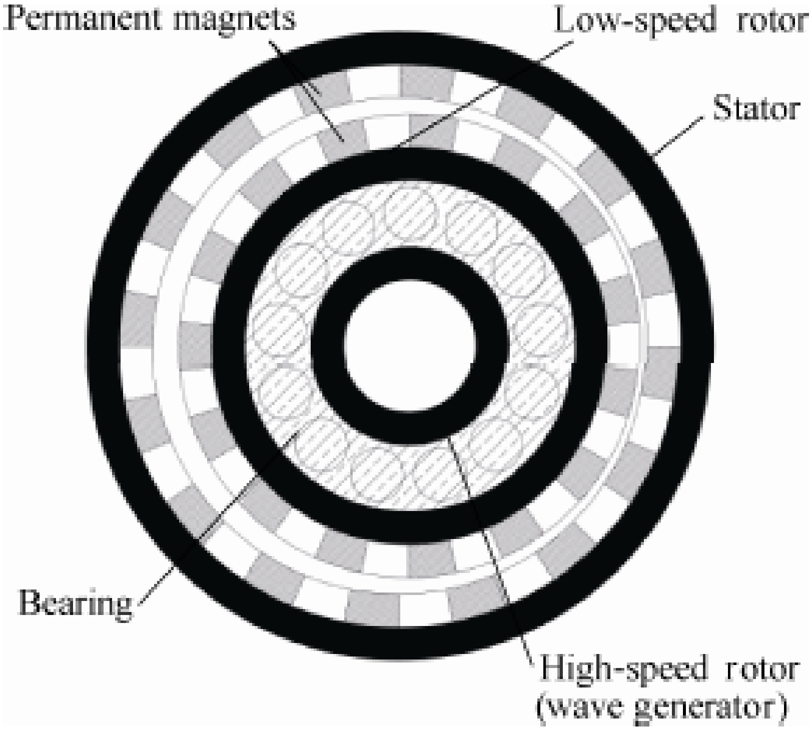

Figure 2.3: Planar representation of an Harmonic MG [1]

The wave generator causes the outer rotor deformation through sliding contact because the low-speed rotor ensures rotational and orbital motion. Moreover, the magnetic field modulation is possible via a variable air gap [4].

2.2 Planetary magnetic gearbox

This gearbox allows using three transmission modes and a high-speed ratio. This structure can also have six transmissions to increase the transmission torque by approximately two [6]. This MG has many advantages, like the facility of production in a fully assembled line. It can be used like:

- a single input or output unit to reduce angular velocity.
- a differential gearbox to allow different transmission ratios.

The base geometrical structure is characterised by

- a carrier;
- five iron yokes;
- a series of outer permanent magnets;
- three magnetic planet gears;
- a magnetic sun gear.

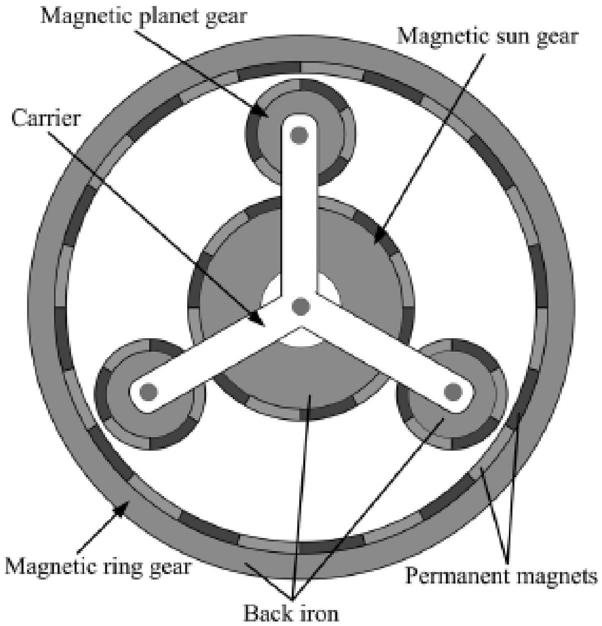

Figure 2.4: Planar representation of a Planetary MG [6]

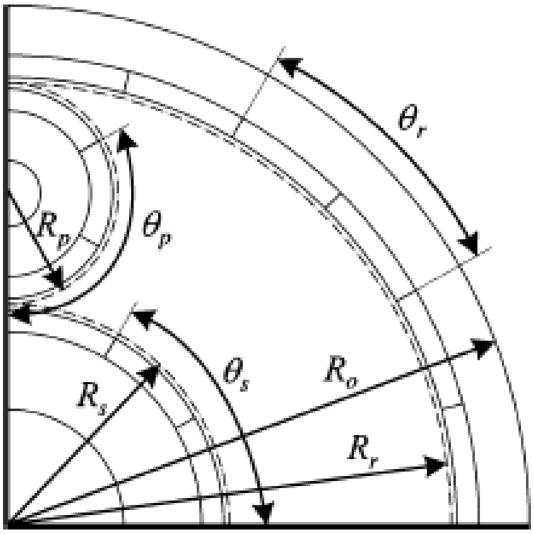

Figure 2.5: Geometrical definition of a Planetary MG [6]

During the project, it is important to avoid phenomena like sliding and the pole slipping. Consequently, the pole pitch angle must be the same for each structure. This means that the following relations must be respected from the article [6]:

$$R_s\theta_s = R_p\theta_p = R_r\theta_r \tag{2.1}$$

Defining the pitch angle as

$$\theta = \frac{2\pi}{P} \tag{2.2}$$

where P define the number of pole pairs, it is possible to define the following ratios:

$$\frac{R_s}{P_s} = \frac{R_p}{P_p} = \frac{R_r}{P_r} \tag{2.3}$$

Another relation to respect is

$$R_s + 2R_p = R_r \tag{2.4}$$

Combining the equations 2.3 and 2.4 this relationship must be respected

$$P_s + 2P_p = P_r \tag{2.5}$$

Chapter 3

Coaxial magnetic gearbox

3.1 Basic structure principles

The CMG is mainly composed by the following parts:

1. an inner yoke used to close the inner PM magnetic field lines;
2. an inner high speed rotor with p_{in} pair of poles;
3. an intermediate ring called modulator characterised by $Q = p_{in} + p_{out}$ ferromagnetic pole pieces;
4. an outer low speed rotor with p_{out} pair of poles;
5. an outer yoke used to close the outer PM magnetic field lines.

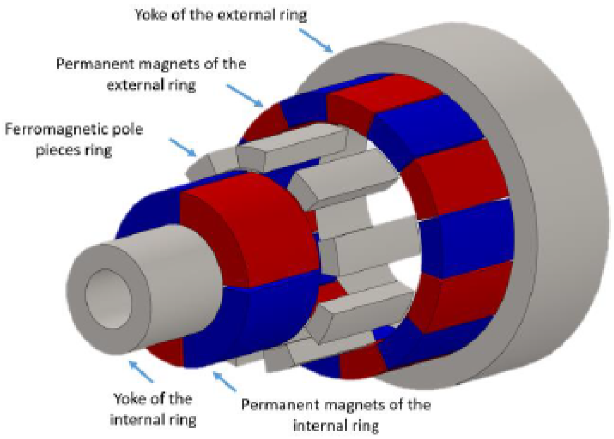

Figure 3.1: Planar representation of a CMG [1]

The relation between the angular speeds is:

$$p_{in}\omega_{in} + p_{out}\omega_{out} = Q\omega_M \tag{3.1}$$

If the modulator is fixed, it is possible to define the gearbox ratio as the inverse of torque ratio. It follows that:

$$\eta = \left|\frac{\omega_{out}}{\omega_{in}}\right| = \left|\frac{T_{in}}{\omega_{out}}\right| = \frac{p_{in}}{p_{out}} \tag{3.2}$$

The torque ratio comes from a power balance, where hysteresis (P_c) and eddy currents losses (P_{ec}) are neglected.

$$T_{in}\omega_{in} - T_{out}\omega_{out} = P_h + P_{ec} \approx 0 \longrightarrow \frac{T_{out}}{T_{in}} = \frac{\omega_{in}}{\omega_{out}} \tag{3.3}$$

In particular the modulator creates low reluctance paths and it allows to obtain the torque from different pairs of poles in the inner and outer rotor. The field interaction between the inner and the outer rotor determines the torque transmission at a different speed.

With $Q = p_{in} + p_{out}$ is demonstrated that torque capabilities are maximum. The modulator effect creates alternately “short-circuit” N-S pole-pairs for each rotor or produce a pole (north or a south) similar to what occurred. [7]

The useful effect of this speed reducer is a result of the interaction between two magnetic fields. In fact, the magnitude of the torque is proportional to the product between the two magnetic fields. If there is a sinusoidal variation of the magnetic flux in the air gap, the torque is in fact proportional to a sinus under a pair of poles. But, if the number of poles between the inner and the outer ring is different, the net torque is zero.

3.2 PM thickness and airgap thickness influence

3.2.1 PM thickness influence

Choosing the right PM thickness brings benefits about the torque capability. In particular, the inner PM rotor is more sensible than the outer one. The figure shows how the PM thickness has an impact in terms of useful torque. Effectively, it doesn't correspond a big advantage in terms of torque capabilities and effectiveness costs.

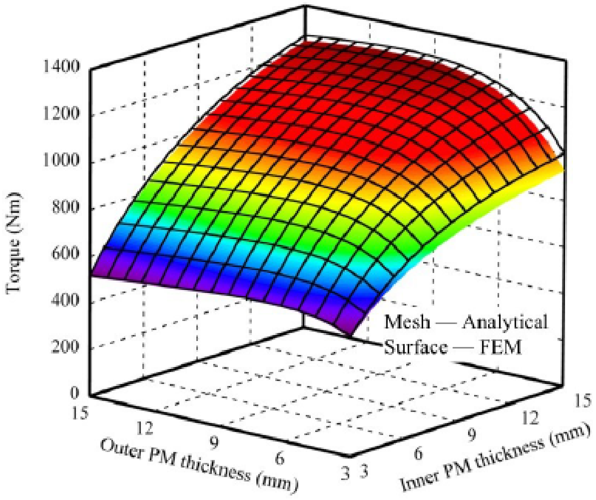

Figure 3.2: Torque capabilities varying the inner or the outer PM thickness [8]

3.2.2 Airgap thickness influence

The airgap values have a big impact in a CMG as they increase the reluctance of the magnetic circuit: with an air gap thickness increase a linear torque decrease is created because of CMG flux tube the reluctance growing up. In fact,the figure shows that the inner and the outer airgap capabilities totally changes. If the airgap is big, there is more flux circuiting between outer PMs and modulation pole-pieces. This increase in leakage flux value doesn't product useful torque effects and a practical rule to limit it is to impose the airgap thickness in the range between 0.6 - 2.4 mm.

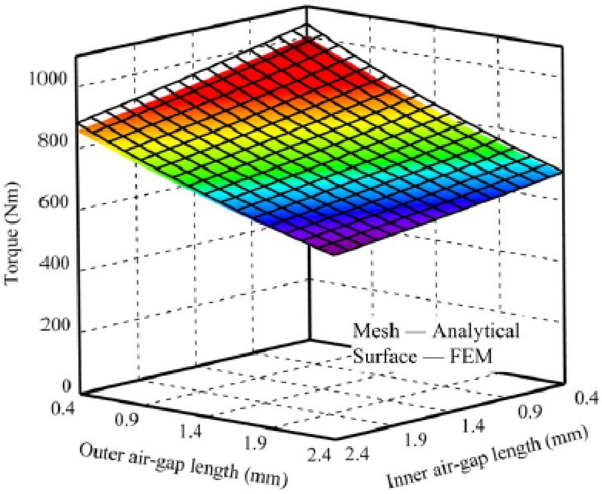

Figure 3.3: Torque capabilities varying the inner or the outer airgap [8]

Chapter 4

Magnetic analysis

4.1 Introduction

This part explains how it is possible to explain how the interaction between the radial and tangential magnetic induction creates a useful torque. To analyze the magnetic induction problem, the MG domain has different layers:

1. the inner rotor layer;
2. the inner air gap layer;
3. the modulator zone;
4. the outer airgap domain;
5. the outer rotor domain.

In order to evaluate the magnetic induction profile, the magneto-static Maxwell equations must be considered and, under these working conditions, the definition of a magnetic vector potential is possible.

4.2 Magneto-static Maxwell Equations

In a quasi magneto-static applications, for the high-speed rotor and the low-speed rotor, to know the flux density the following equations must be defined:

$$\nabla \times \mathbf{H} = J \tag{4.1}$$

$$\nabla \times \mathbf{E} = -\frac{\partial \mathbf{B}}{\partial t} \tag{4.2}$$

$$\nabla \bullet \mathbf{B} = 0 \tag{4.3}$$

$$\nabla \bullet \mathbf{D} = \rho \tag{4.4}$$

where **H** is the magnetic field , **B** is the magnetic induction , **E** is the electric field and ρ is the volume density of charge. The magnetic induction **B** is derived from H via the magnetic permeability ($\mathbf{B} = \mu\mathbf{H}$), and the electric induction vector **D** is related to the electric field **E** via the dielectric constant material ϵ ($\mathbf{D} = \epsilon\mathbf{E}$) [9]. The equation 4.1 defines the curl of H equal to the current density J and the 4.4 the divergence of B equal to zero. These two pieces of information, combined, define the magnetic field properties. B's divergence defines the potential magnetic vector **A**, which means that the magnetic field lines tend to be close. In terms of differential equations, the B solenoidality can be written as

$$\nabla^2 A = 0 \tag{4.5}$$

Thanks to the hypothesis of two dimensional field distribution, that is that fields values are independent on the third spatial coordinate z, the magnetic vector potential A has only one component different from 0 and thus it can be considered as $A_z = A_z(x, y)$.
The electrical field, instead, has a link with the Faraday-Neumann law. Considering a closed line in a circuit (e.g., a turn), the electric field's close integration is not zero, and it is equal to the time derivative of the magnetic flux in a turn. This means that a flux variation in the time, due to a relative movement between the magnetic field and the circuit or to the magnetic field variation, corresponds to an induced electromotive force.

As a consequence, it is impossible to define a scalar electric potential like in the electrostatic case (in this case, E is irrotational). The problem is solved with the introduction of the potential magnetic vector A defined as

$$\mathbf{B} = \nabla \times \mathbf{A} \tag{4.6}$$

4.3 CMG problem definition

To know the torque, it is important to evaluate the radial magnetic induction B_r and the tangential magnetic induction B_t in the inner and outer air gap. This leads to an analytical planar model with cylindrical coordinates: the radius r and the rotor angular position θ.
The magnetic induction produced by the permanent magnets for the inner and the outer rotor is a alternate wave. This waveform develops in Fourier series as the sum of infinite harmonics expressed by the following equation:

$$B_{pm} = \sum_{n=1}^{+\infty} B_{r,h} \sin n(\theta - \varphi) \tag{4.7}$$

where

$$B_{r,h} = \begin{cases} \frac{4B_r p}{\pi h}, & \text{if } h \text{ is odd} \\ 0, & \text{if } h \text{ is even} \end{cases} \tag{4.8}$$

p is the pair of poles number,θ is the rotor position and φ is the initial rotor position. The analytical model used to do the magnetic induction evaluation is based on the following assumptions:

- end effects are neglected;
- permeability of the iron is infinite (the magnetic field in the iron vanishes);
- relative recoil permeability of the magnets is $\mu_r = 1$.

The two dimensional cross section of the model is as follows:

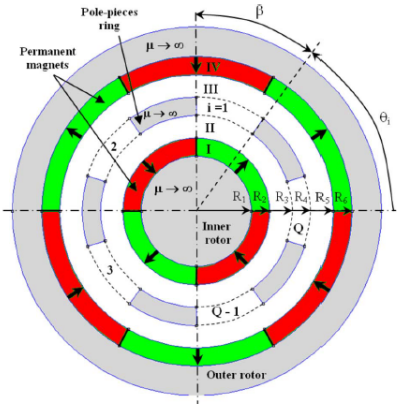

Figure 4.1: Planar vision of the CMG [1]

With those assumptions, a Laplace (or Poisson) must be solved to find a close solution for the Potential Magnetic Vector. In particular, for 2D studies A can be assumed as a scalar with the following equations:

$$\nabla^2 A = \frac{\partial B_{pm}}{r \partial \theta} \tag{4.9}$$

for the inner and outer PM layer

$$\nabla^2 A = 0 \tag{4.10}$$

for the two air gaps and the modulator.
For each layer to guarantee continuity, the following boundary conditios must be imposed

- Dirichlet condition: the condition is linked to have an established value for the potential magnetic vector;
- Neumann condition: it is linked to the A first derivative (the magnetic induction field);
- Robin condition: it is linked to mixed condition between the Dirichlet and Neumann condition.

The radial and tangential magnetic induction define the scalar magnetic potential, and it follows that [10]:

$$B_{r,i} = \frac{1}{r} \frac{\partial A_i}{\partial \theta} \tag{4.11}$$

$$B_{t,i} = -\frac{\partial A_i}{\partial r} \tag{4.12}$$

4.3.1 Inner and outer PM layer

In this case, the differential equation to solve is of Poisson type

$$\frac{\partial^2 A_i}{\partial r^2} + \frac{1}{r}\frac{\partial A_i}{\partial r} + \frac{\partial^2 A_i}{\partial \theta^2} = \frac{1}{r}\frac{\partial B_{pm}}{\partial \theta} \tag{4.13}$$

where i = I,V and it refers to the inner and outer PM layers. The general solution can be found using the variable separation method and the superposition method (equation 4.14). Consequently, the general solution is like in reference [8].
For the inner PM the general solution is:

$$\begin{aligned} A_I(r,\theta) &= \sum_{n=1}^{+\infty} [A_n^I r^n + B_n^I r^{-n} + X_n(r)\cos(n\varphi_i)]\cos(n\theta) \\ &+ \sum_{n=1}^{+\infty} [C_n^I r^n + D_n^I r^{-n} + X_n(r)\sin(n\varphi_i)]\sin(n\theta) \end{aligned} \tag{4.14}$$

where A_n^I, B_n^I, C_n^I, D_n^I are general integration constants associated to the homogeneous partial differential equation, and X_n is a particular solution.
X_n can be expressed as it follows:

$$X_n(r) = \begin{cases} \frac{4B_r p_{in} r}{\pi(1-n^2)}, & \text{if n = j p}_{in},\ j = 1,3,5... \\ \frac{2B_r r \ln(r)}{\pi}, & \text{else if n = p}_{in} = 1 \\ 0, & \text{otherwise} \end{cases} \tag{4.15}$$

For the outer PM, the general solution is similar:

$$\begin{aligned} A_V(r,\theta) &= \sum_{n=1}^{+\infty} [A_n^V r^n + B_n^V r^{-n} + X_n(r)\cos(n\varphi_i)]\cos(n\theta) \\ &+ \sum_{n=1}^{+\infty} [C_n^V r^n + D_n^V r^{-n} + Y_n(r)\sin(n\varphi_o)]\sin(n\theta) \end{aligned} \tag{4.16}$$

The meaning of each coefficient is the same as in the equation (3.15) and the particular coefficient for each harmonic is:

$$Y_n(r) = \begin{cases} \frac{4B_r p_{out} r}{\pi(1-n^2)}, & \text{if n = j p}_{out},\ j = 1,3,5... \\ \\ \frac{2B_r r \ln(r)}{\pi}, & \text{else if n = p}_{out} = 1 \\ \\ 0, & \text{otherwise} \end{cases} \tag{4.17}$$

The boundary conditions are mixed, and they impose the continuity of the magnetic potential and the derivative condition equal to zero, between the first and the second layer, and the forth and the fifth layer.

$$Y_n(r) = \begin{cases} A_I(r_2,\theta) = A_{II}(r_2,\theta) \\ \frac{\partial A_I}{\partial r}|_{r=r_1} = 0 \\ A_{IV}(r_5,\theta) = A_V(r_5,\theta) \\ \frac{\partial A_V}{\partial r}|_{r=r_6} = 0 \end{cases} \tag{4.18}$$

The two Dirichlet conditions impose the A continuity between the inner PM and the inner airgap and between the outer air gap and the outer PM. The other two Neumann conditions, instead, indicate that the tangential magnetic induction for $r = r_1$ and $r = r_6$ is zero.

4.3.2 Inner and outer airgap

The general solution comes from equation 4.10. This relation is a partial derivative homogeneous equation, and there are not associated with particular solutions. For the inner and the outer airgap, the solution of the magnetic potential is written as it follows [8]:

$$A_{II}(r,\theta) = \sum_{n=1}^{+\infty}(A_n^{II}r^n + B_n^{II}r^{-n})\cos(n\theta) + \sum_{n=1}^{+\infty}(C_n^{IV}r^n + D_n^{IV}r^{-n})\sin(n\theta) \quad (4.19)$$

$$A_{IV}(r,\theta) = \sum_{n=1}^{+\infty}(A_n^{IV}r^n + B_n^{IV}r^{-n})\cos(n\theta) + \sum_{n=1}^{+\infty}(C_n^{IV}r^n + D_n^{IV}r^{-n})\sin(n\theta) \quad (4.20)$$

The coefficients $A_n^{II}, B_n^{II}, C_n^{II}, D_n^{II}, A_n^{IV}, B_n^{IV}, C_n^{IV} and D_n^{IV}$ are found imposing the right boundary conditions that suits to the physical problem. The boundary conditions are based on the continuity of the tangential magnetic induction. Concerning the interface between the inner PM and the inner airgap

$$\frac{\partial A_I}{\partial r}|_{r=r_2} = \frac{\partial A_{II}}{\partial r}|_{r=r_2} \quad (4.21)$$

$$\frac{\partial A_{IV}}{\partial r}|_{r=r_5} = \frac{\partial A_V}{\partial r}|_{r=r_5} \quad (4.22)$$

Between the inner airgap and the modulator, instead, the alternation between the air and the modulator cannot be neglected. In fact, in the iron slot the tangential induction is zero while in the air zone has a particular wave $f(\theta)$ in analytic evaluations called Sturm-Liouville problem in an annulus [1].

$$f(\theta) = \begin{cases} \frac{\partial A_{III,i}}{\partial r}, & \text{in the air slots} \\ \\ 0, & \text{in the iron slots} \end{cases} \quad (4.23)$$

4.3.3 Modulator

The equation to solve is the following:

$$\frac{\partial^2 A_{III,i}}{\partial r^2} + \frac{1}{r}\frac{\partial A_{III,i}}{\partial r} + \frac{1}{r^2}\frac{\partial^2 A_{III,i}}{\partial \theta^2} = 0 \tag{4.24}$$

for

$$\begin{cases} r_2 \leq r \leq r_3 \\ 0 \leq \theta \leq 2\pi \end{cases} \tag{4.25}$$

In this case the radial magnetic induction for the interface between the air and the iron slot is zero.

$$\frac{\partial A_{III,i}}{\partial \theta}|_{\theta=\theta_i} = \frac{\partial A_{III,i}}{\partial \theta}|_{\theta=\theta_i+\beta} = 0 \tag{4.26}$$

where i is i-th slot and β is the slot angle. Moreover, the magnetic scalar potential is continuous between the inner airgap and the modulator, and the modulator and the outer airgap.

$$A_{II}(r_3, \theta) = A_{III,i}(r_3, \theta) \tag{4.27}$$

$$A_{III,i}(r_4, \theta) = A_{IV}(r_4, \theta) \tag{4.28}$$

Applying the border conditions (3.26,3.27,3.28) the scalar magnetic potential is

$$A_{III,i}(,\theta) = A_0^i + B_0^i \ln r + \sum_{n=1}^{+\infty} [A_n^{III,i}(\frac{r}{r_4})^{\frac{n\pi}{\beta}} + B_n^{III,i}(\frac{r}{r_3})^{\frac{-n\pi}{\beta}}] \cos\frac{n\pi}{\beta}(\theta - \theta_i) \tag{4.29}$$

The border conditions joined together form a linear equation system of size $l = 12n + 2Q(1 + K)$, where:

- i is the harmonic order for the inner and outer PM magnetic induction;
- Q is the slot number;
- k is the harmonic order for the modulator magnetic induction.

4.4 Static torque calculation

The static torque calculation takes into account the interaction between the radial and the tangential magnetic induction in the inner and outer airgap. This type of analysis depends on how the magnetic energy in the airgap changes using the Maxwell tensor approach. In a linear material, the force density using the Lorentz approach is described as it follows:

$$f = J \times B - \frac{1}{2}H^2 grad\mu \tag{4.30}$$

This volumetric force can be expressed as the Maxwell torque tensor divergence.

$$f = J \times B - \frac{1}{2} H^2 grad(\mu) \tag{4.31}$$

Applying the Gauss theorem and considering the middle circumference in the inner and in the outer airgap, the static torque in an analytical and numerical approach is expressed in the following way [11], [8]

$$T_{in} = \frac{l_{ax} r_{int}^2}{\mu_0} \int_0^{2\pi} B_{r,in} B_{t,in} d\theta \tag{4.32}$$

$$T_{out} = \frac{l_{ax} r_{out}^2}{\mu_0} \int_0^{2\pi} B_{r,out} B_{t,out} d\theta \tag{4.33}$$

where l_{ax} is the axial length, r_{in} is the medium inner airgap radius, r_{out} is the medium outer airgap radius, $B_{r,in}$ is the inner radial magnetic induction, $B_{t,in}$ is the tangential magnetic induction, $B_{r,out}$ is the outer radial magnetic induction and $B_{t,out}$ is the outer tangential magnetic induction.

Chapter 5

Simulation results

5.1 Context

The work purpose is to analyse the CMG against the planetary mechanical gear for an aircraft accessory unit. In the architecture if a component fails, all the distribution is out of use. The transmission starts from the Air Starter turbine (ATS). To this unit it corresponds an input angular speed $\omega_{in} = 14560$ rpm. In the left zone, there are a fuel pump and a permanent magnet alternator. In the right zone, there is the oil pump unit (OPU), the integrated drive generator (IDG) and the hydraulic pump (HP). The simulation aims is to understand how the static torque characteristic has an impact to size the CMG. The analysis has a focus on the oil pump and the other components, to remove a standard planetary mechanical

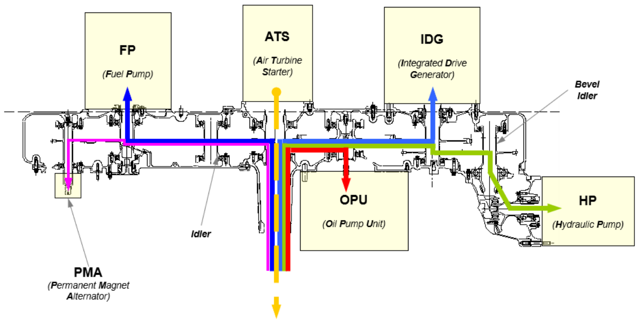

Figure 5.1: Aircraft accessories structure

gear. The components to identify in the fig 5.2 are:

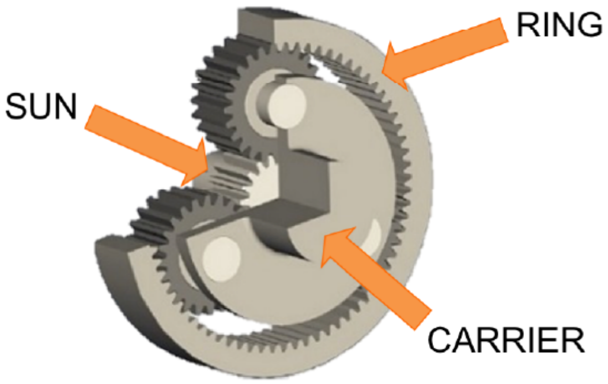

Figure 5.2: Planetary mechanical gear [12]

- the internal sun gear;
- the external ring gear;
- an intermediate structure called carrier characterised by generally three planet gears

Each component has his equivalence reported to the CMG structure. The sun act as the high speed rotor; the carrier acts as a modulator and the planet as a low speed rotor. [12]

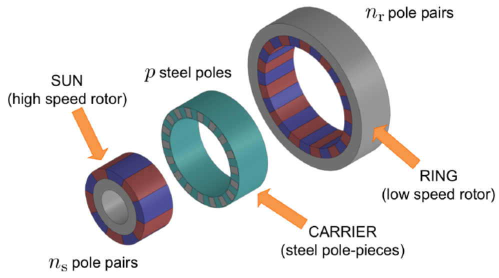

Figure 5.3: CMG correspondance [12]

The transmission ratio in a mechanical context is defined from two wheels: a driving wheel and a driven wheel. Given the number of teeth of the driven wheel d_2 and the number of teeth of the conducting wheel d_1 as mechanical specifications, the transmission ratio η is defined according to the following equation

$$\eta = \frac{d_2}{d_1} = \left|\frac{\omega_{out}}{\omega_{in}}\right| \tag{5.1}$$

In the electromagnetic context, the transmission ratio is equal to the transfer speed function. In this case, the system is a reducer because $\eta \leq 1$.

5.2 MG sizing

Before the analysis result, the first step was to define the CMG design model and a sizing strategy with the specifics resumed in the table.

Geometrical parameter	Definition
B_{sf}	Saturation magnetic induction: 1.5 T
B_m	Residual magnetic induction: 1.2 T
r_1 to r_8	From internal to external radius
l_{ax}	axial length: 25 mm
l_{air}	airgap thickness: 1 mm
p_{in}	internal rotor pair of poles
p_{out}	external rotor pair of poles
l_m	permanent magnet thickness
l_{in}	internal yoke thickness
l_{out}	external yoke thickness
l_{mod}	modulator thickness

Table 5.1: Geometrical parameters

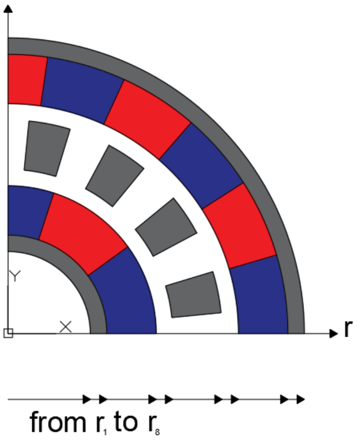

Figure 5.4: CMG geometry

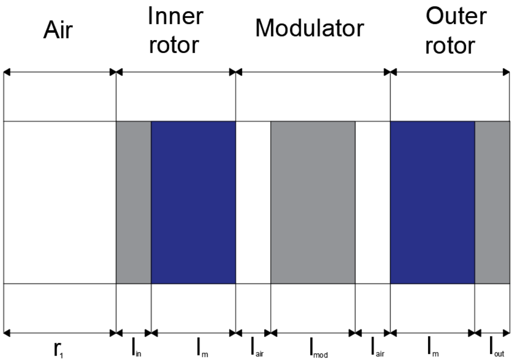

Figure 5.5: CMG cross section

From the specifics, the external radius r_8 is known imposing the axial length and the volumetric torque. Developing a sizing strategy for the PM thickness and the modulator thickness, it is possible to define all the CMG characteristics.

5.2.1 Internal and external yoke sizing

Two sizing approaches are possible to determine the inner and outer yoke thickness:

- a global approach with simplified hypothesis;
- a local approach to have a local precise flux evaluation.

The relation to respect for both approaches is

$$\int_S B_r(r,\theta)dS \leq \int_{S_m} B_{t,yoke}dS_m \tag{5.2}$$

where B_r is the radial PM magnetic induction, $B_{t,yoke}$ is the maximum tangential magnetic induction, S is the PM normal surface, and S_m is the tangential yoke surface. This equation means that the magnets' radial flux must be lower than the maximum circular yoke crowns' tangential flux.

The local approach needs the radial magnetic induction and the maximum tangential yoke flux profile, and to retrieve this information analytically is complicated.

With the global approach, problem simplifications are useful to obtain similar results. In this case, the problem to solve is characterised by a magnet attached to a simple yoke, for example.

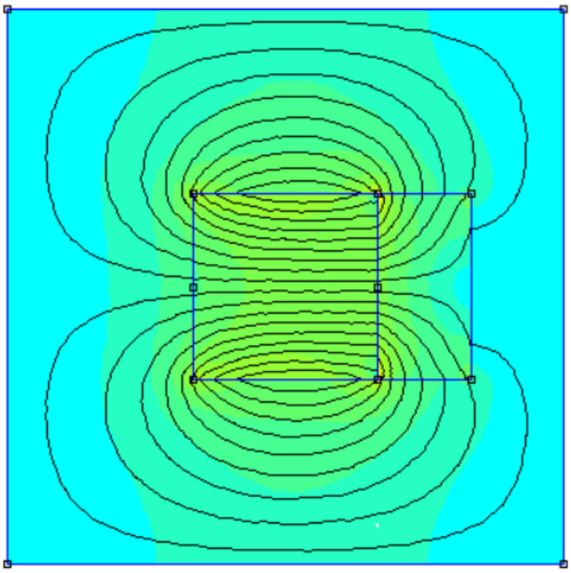

Figure 5.6: A PM joined an Iron yoke

It happens that the radial PM field lines close symmetrically into the two yoke tangential surfaces. Supposing a uniform radial magnetic induction B_m with multiplicity equal to p_{in} in 360 degrees of angular rotor space and neglecting the slot effects into the modulator structure, it follows that:

$$B_m \frac{pi}{2p_{out}} r_2 l_{ax} \leq B_{sf} l_{in} l_{ax} \rightarrow l_{in} \geq \frac{B_m}{B_{sf}} \frac{pi}{2p_{out}} r_2 \tag{5.3}$$

For the outer yoke, the reference radius r_8 allows to evaluate l_{out} because if $r_8 \gg l_{out} \rightarrow r_7 \approx r_8$. It follows that to avoid the saturation in the yoke, the minimum outer yoke thickness is:

$$l_{out} \geq \frac{B_m}{B_{sf}} \frac{\pi}{2p_{out}} r_8 \tag{5.4}$$

If the radial magnetic induction is analytically known, with the local approach the surface integral becomes a simple line integral:

$$l_{in} \geq \frac{\int_0^{\frac{\pi}{2p_{in}}} B_m(r,\theta) r d\theta}{B_{sf}} \tag{5.5}$$

$$l_{out} \geq \frac{\int_0^{\frac{\pi}{2p_{out}}} B_m(r,\theta) r d\theta}{B_{sf}} \tag{5.6}$$

The global approach, neglecting the air slot effect, gives an excess evaluation. In the local approach instead, the thickness is less than the previous case because the Fourier magnetic induction has a finite harmonics number and there some holes in the radial magnetic induction profile.

5.2.2 Modulator thickness

The strategy used to size the modulator thickness is to consider the maximum tangential induction. An example to understand the phenomena is characterised by an iron slot between two PMs polarised in the opposite direction.

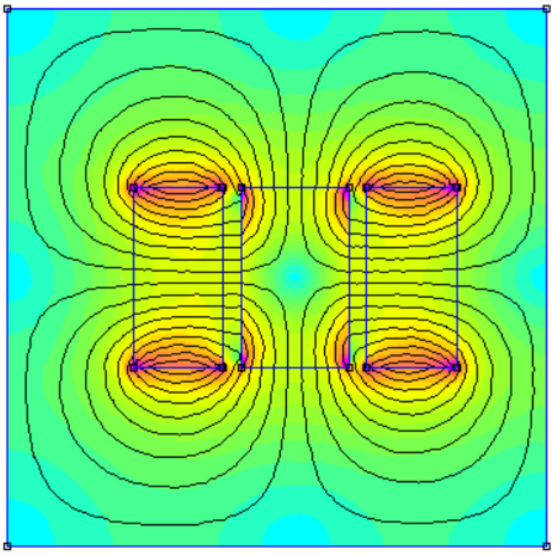

Figure 5.7: An iron slot between two PMs

From the figure 5.7 the field lines hit the modulator radially, and then they deflect on the tangential modulator surface. Dividing the iron slot into four equal surfaces the situation is equal. If a quarter of iron slot is considered, with a magnetic induction of amplitude B_m the modulator thickness can be retrieved in the following way

$$B_m \frac{\beta r_5}{2} l_{ax} \leq B_{sf} \frac{l_{mod}}{2} l_{ax} \rightarrow l_{mod} \geq \frac{B_m}{B_{sf}} \beta r_5 \tag{5.7}$$

where β is the iron slot angle.

5.3 First approach

The first approach considers some quantities like the mechanical power P and the outer rotor volumetric torque T_v. Analyzing the oil pump case, the output speed is $\omega_{out} = 6820.9$ rpm and the input speed is $\omega_{in} = 14560$ rpm. In this way, the transmission ratio is $\eta = \frac{p_{in}}{p_{out}} = 0.47$.
The first step is to choose the right pair of poles combination's, giving priority to minimize the torque ripple. To guarantee this condition, it is necessary to choose the right structure that has the minimum common multiple N_{mc} between the inner pair of poles p_{in} and the number of ferromagnetic slots Q [**12**]. This is also an indicator of the fundamental cogging torque harmonic.

	1^{st} config	2^{nd} config	3^{rd} config	4^{th} config
p_{in}	5	6	11	17
p_{out}	11	13	23	37
Q	16	19	34	54
N_{cm}	80	114	374	918
η	0.45	0.46	0.47	0.46

Table 5.2: Pair of poles combinations and transmission ratio resume

The CMG external radius r_{ext} is known imposing the volumetric torque T_v and considering the external magnetic gearbox volume like in the reference [13].

$$T_v = \frac{T_{out}}{\pi r_{ext}^2 l_{ax}} = \frac{P}{\omega_{out} \pi r_{ext} l_{ax}} \rightarrow r_{ext} = \sqrt{\frac{P}{T_v \pi \omega_{out} l_{ax}}} \tag{5.8}$$

The total power is the sum of the demanded power peaks on the right branch by the IDG, OPU and the HP.

$$P = P_{IDG} + P_{OPU} + P_{HP} = (20880 + 74570 + 56673)W = 152123W \tag{5.9}$$

The inner and outer yoke thickness, and the modulator thickness has the same sizing strategy discussed in the chapter 6.2.

	1_{st} config	2_{nd} config	3_{rd} config	4_{th} config
p_{in}	5	6	11	17
p_{out}	11	13	23	37
Q	16	19	34	54
r_{ext}	118.04 mm	122.23 mm	108.06 mm	103.14 mm
l_{in}	8.11 mm	15.2 mm	7.78 mm	5.77 mm
l_{out}	27.15 mm	22.98 mm	12.99 mm	8.07 mm
l_m	10.06 mm	8.51 mm	4.81 mm	2.99 mm
r_{int}	62.9 mm	57.36 mm	60.31 mm	72.31 mm

Table 5.3: First geometrical sizing approach

Knowing all the geometric data, a planar cylindrical model design was created to run the FEMM model. The geometric parameters come from a sizing function and the model assumptions are:

- Use of linear iron with μ_r =1000;
- Use of a real PM material (NbFeB N35, Br=1.2 T).

To get a closer real MG model, circular yokes have been considered as a mechanical support for the permanent magnet system. Considering the single layer boundary is not simple. The simplest solution is to confine the MG system in a square and to set A=0 in the external border. But this strategy creates a lot of supplementary mesh elements, and there are a lot of numerical errors like in this static torque

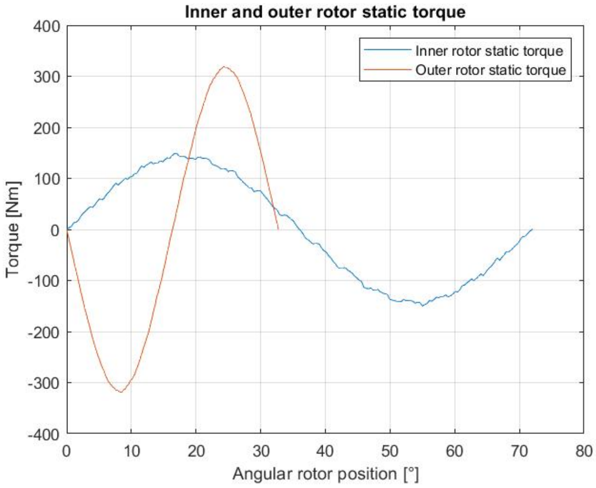

Figure 5.8: Example of static torque characteristic with $p_{in} = 5$ and $p_{out} = 11$

characteristic. Moreover, this model has big dimensional differences with the mechanical gear considered.

5.4 Second approach

To do a valid comparison with the CMG, the oil pump gears parameters has been taken as a reference. In particular, the band diameter is the equivalent of the outer diameter and the axial length corresponds to the thickness of the gear wheel. With r_{ext} = 141 mm and l_{ax} = 28 mm, the geometrics characteristic are in this table.

	1^{st} config	2^{nd} config	3^{rd} config	4^{th} config
p_{in}	5	6	11	17
p_{out}	11	13	23	37
r_{int}	60.53 mm	69.06 mm	91.92 mm	104.02 mm
l_{out}	20.13	17.04	9.63	5.99
l_{in}	20.31 mm	18.29 mm	11.86 mm	8.31 mm
l_m	26.01 mm	22.61 mm	13.59 mm	8.7 mm
T_{out}	107.28 Nm	124.51 Nm	179.34 Nm	205.39 Nm
T_{in}	49.51 Nm	57.45 Nm	85.68 Nm	94.58 Nm
m	15.94 kg	14.91 kg	11.49 kg	9.32 kg
$T_{v,in}$	34.7 kNm/m^3	43.2 kNm/m^3	85.2 kNm/m^3	118.6 kNm/m^3
$T_{v,out}$	75.2 kNm/m^3	93.7 kNm/m^3	178.4 kNm/m^3	257.7 kNm/m^3
$T_{v,in}/T_{v,out}$	0.46	0.46	0.48	0.46

Table 5.4: Second approach geometrical data

The table shows how the mass, the torque and the density torque change increasing p_{in}. The mass decrease approximately with a $1/\sqrt{p_{in}}$ behaviour having a fixed η.

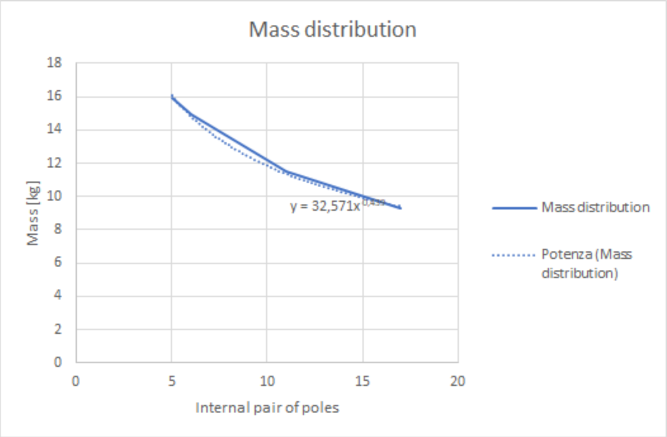

Figure 5.9: Mass distribution with η fixed

The volumetric torque increases of 3.5 times considering the difference between the first and the forth configuration.
Neglecting iron losses (hysteresis and eddy current losses), it follows that the magnetic energy is the same as the mechanical energy for each rotor. This model's border condition is of Neumann type because the iron yokes cannot close all the field lines. In this FEM representation, there is moderated saturation with peaks of 1.5 T except for the model that has p_{in}= 11. In this case, there are small zones where the maximum magnetic induction is 2.2 T. The radial magnetic induction profiles into the inner and the outer airgap respects the pair of poles multiplicity, but it has some holes because of the air slot presence in the modulator. Moreover, the outer airgap has a higher magnetic induction caused by the radial lines that overcome the modulator. The tangential magnetic induction behaviour is difficult to understand because there are some oscillations in the iron zone.

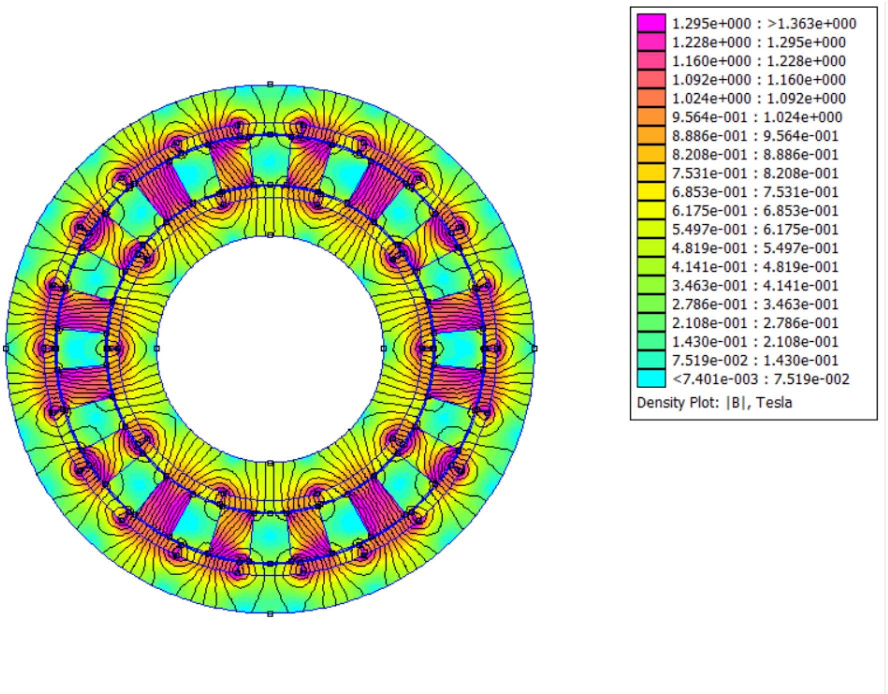

Figure 5.10: FEM plot with $p_{in} = 5$ and $p_{out} = 11$

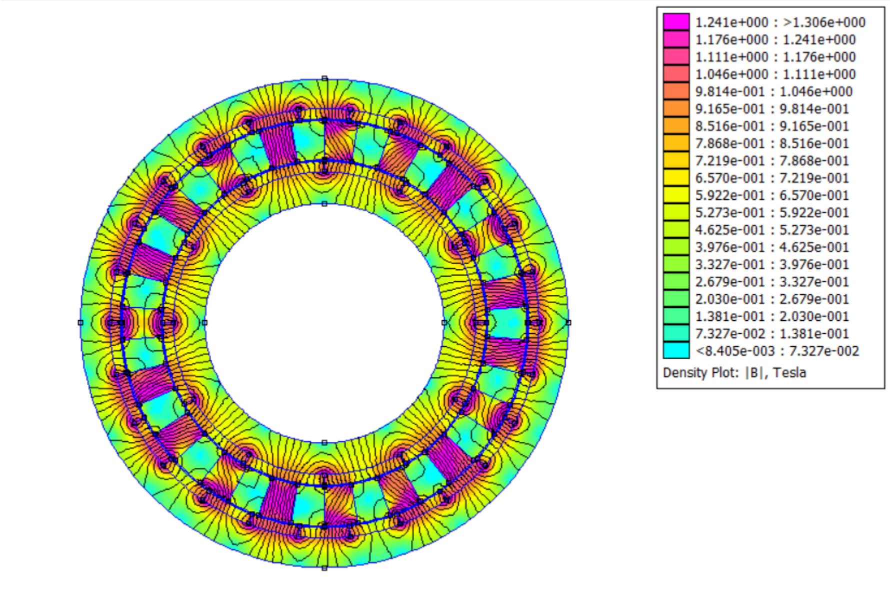

Figure 5.11: FEM plot with $p_{in} = 6$ and $p_{out} = 13$

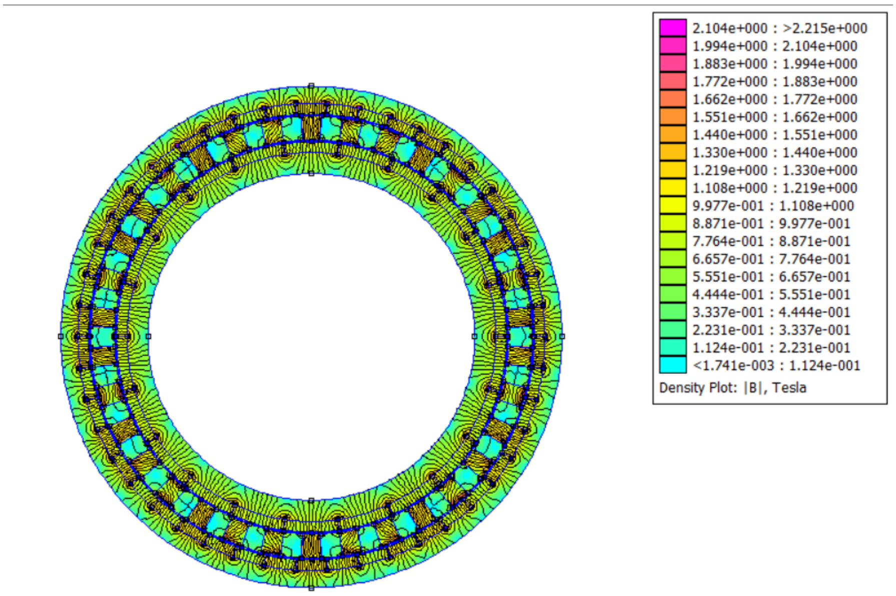

Figure 5.12: FEM plot with $p_{in} = 11$ and $p_{out} = 23$

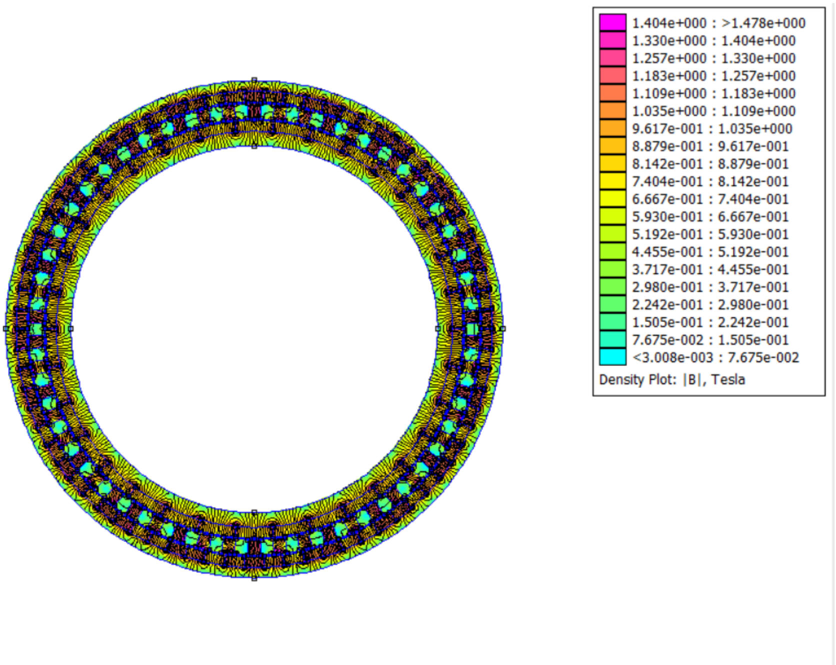

Figure 5.13: FEM plot with $p_{in} = 17$ and $p_{out} = 37$

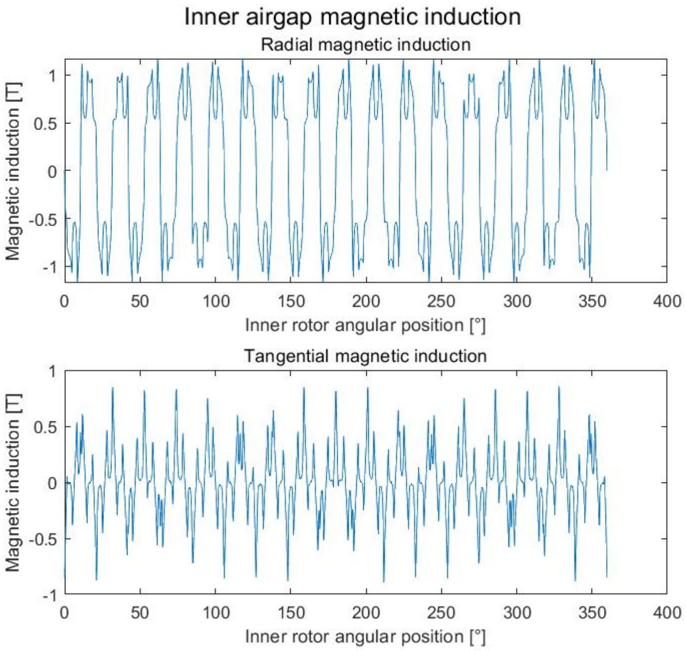

Figure 5.14: Inner airgap magnetic induction plot with $p_{in} = 17$ and $p_{out} = 37$

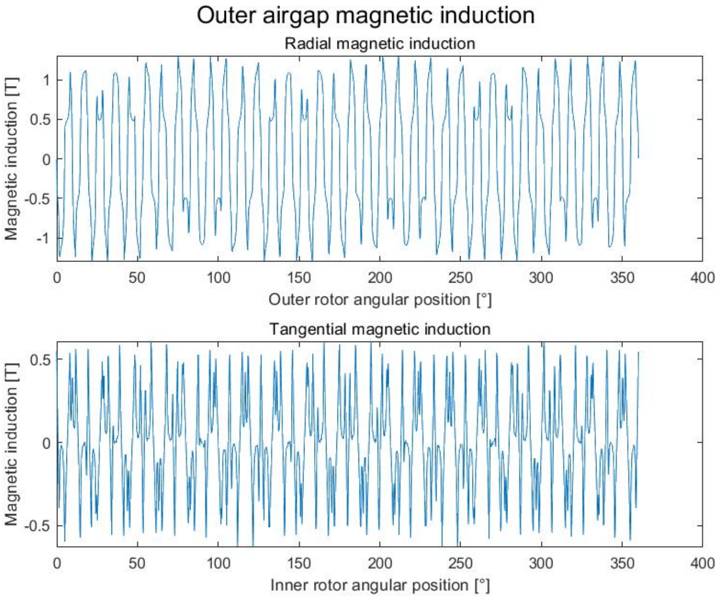

Figure 5.15: Outer airgap magnetic induction plot with $p_{in} = 17$ and $p_{out} = 37$

With the static torque characteristics, the ripple is less important because the mesh model changes for every each CMG model. In particular, it corresponds a higher resolution when the interface for each layer is reduced. Finally the static torque peaks increases if p_{in} increases, and this means that with a lower occupation of useful volume the machine has an higher density torque.

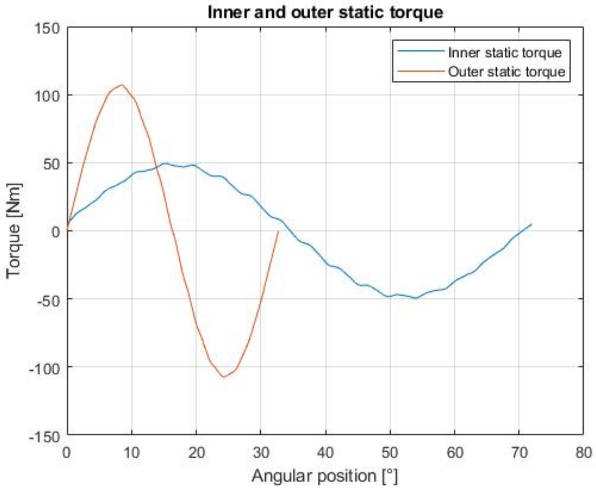

Figure 5.16: Static torque characteristics with $p_{in} = 5$ and $p_{out} = 11$

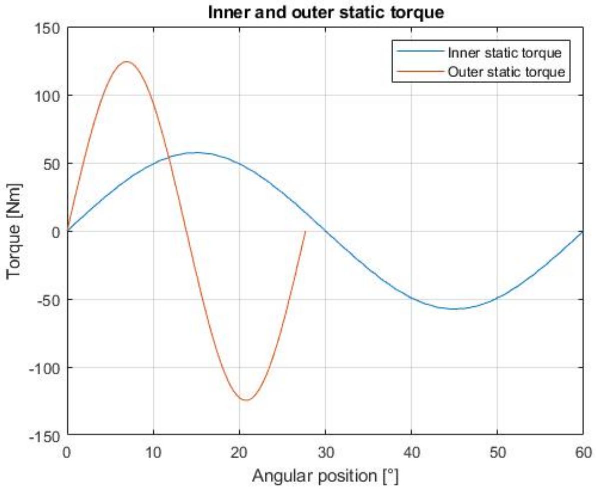

Figure 5.17: Static torque characteristics with $p_{in} = 6$ and $p_{out} = 13$

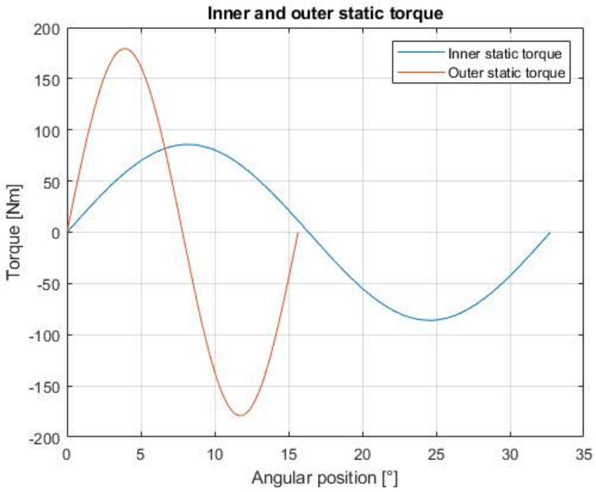

Figure 5.18: Static torque characteristics with $p_{in} = 11$ and $p_{out} = 23$

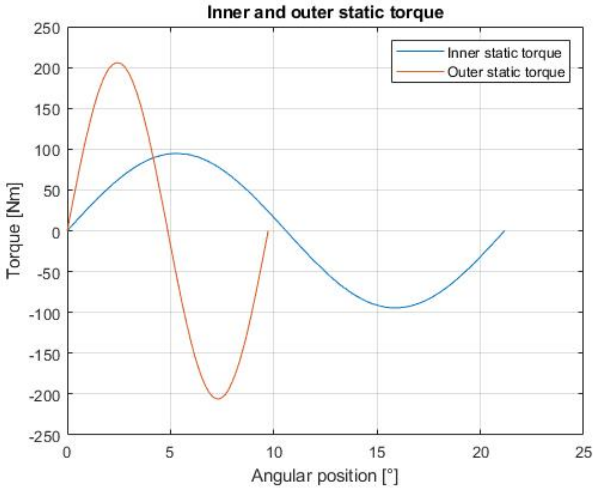

Figure 5.19: Static torque characteristics with $p_{in} = 17$ and $p_{out} = 37$

5.5 Parametric analysis

The parametric analysis has the aim to understand the torque varies in function of multiple variables (p_{in},p_{out},r_{ext}) having the PM thickness, the airgap thickness, the axial lenght l_{ax} and the trasmission ratio fixed. The following characteristics show how the volumetric torque and the torque peaks vary.
The figure 5.20 shows that if the external CMG radius increases the volumetric torque distribution tends to be linear (e.g. r_8 =200 mm).

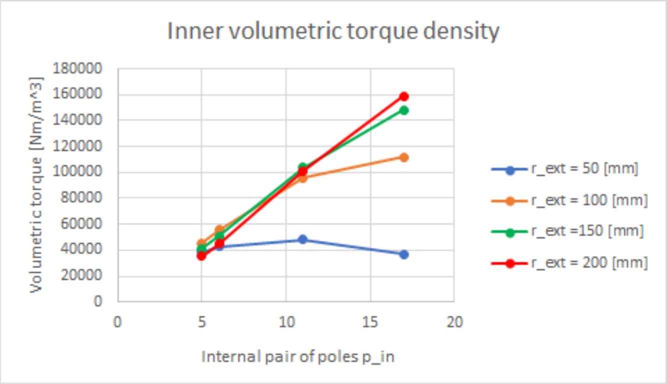

Figure 5.20: Volumetric torque characteristics

The figure 5.21 shows the static torque peaks for p_{in} and l_{ax} fixed. In this case, the torque peaks have a quadratic behaviour for both rotors. It follows that the CMG torque is proportional to the volume occupied because all the studies are planar (2D)

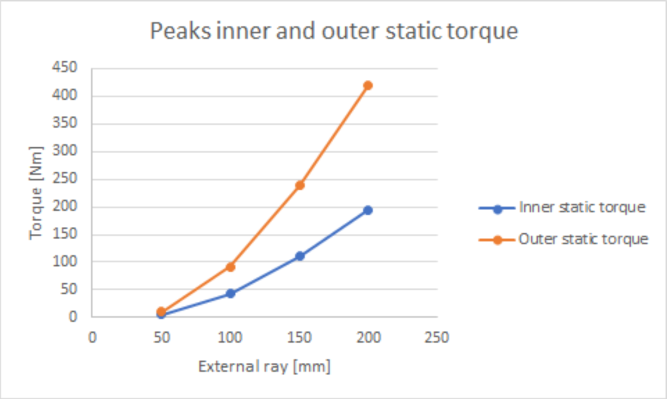

Figure 5.21: Torque rotor peaks characteristics for $p_{in} = 17$

5.6 Non linear case

To conduct non linear analysis, the CMG chosen is characterised by the geometric references resumed in this table.

Geometrical parameter	Value
p_{in}	17
p_{out}	37
r_1	71.89 mm
r_2	77.62 mm
r_3	83.62 mm
r_4	84.62 mm
r_5	88.75 mm
r_6	89.75 mm
r_7	95.75 mm
r_8	100 mm
l_{ax}	25 mm
l_{air}	1 mm
l_m	6 mm
l_{in}	5.74 mm
l_{out}	4.25 mm
l_{mod}	4.13 mm
Useful Volume	$3.8 * 10^{-4}$ m^3
Mass	2.5 kg

Table 5.5: CMG geometrical definition

	Linear iron	Carpenter Silicon Core Iron	M 26 Steel
T_{in}	42.52 Nm	42.73 Nm	42.6 Nm
T_{out}	91.88 Nm	92.07 Nm	91.79 Nm
η	0.46	0.46	0.46
Inner vol torque	112.03 kNm/m^3	112.45 kNm/m^3	112.11 kNm/m^3
Inner mass torque	16.95 Nm/kg	17.09 Nm/kg	17.04 Nm/kg
Outer vol torque	242.09 kNm/m^3	242.29 kNm/m^3	241.55 kNm/m^3
Outer mass torque	36.64 Nm/kg	36.83 Nm/kg	36.71 Nm/kg

Table 5.6: CMG torque performances

With the same geometrical parameters used in the parametric approach, there are not big differences. The analysis uses two Fe-Si alloys characterised by two knees work point:

- 1.5 T for the Carpenter Silicon Core Iron;

- 2.0 T for the M-36 Steel.

From the figures 5.22 and 5.23, the magnetic induction peaks do not have big differences. But the working point in the DC magnetisation curve change:

- the Carpenter Silicon Core Iron works next to the working point ;

- the M-36 Steel works in a point that belongs to the linear characteristics.

The gearbox that gives the best performances is the Carpenter Core Iron because the material works it gives best value of mass and volumetric torque. For the linear iron the transmission ratio is next to the ideal ratio because the two non linear materials has a numerical modeling of their real characteristics.

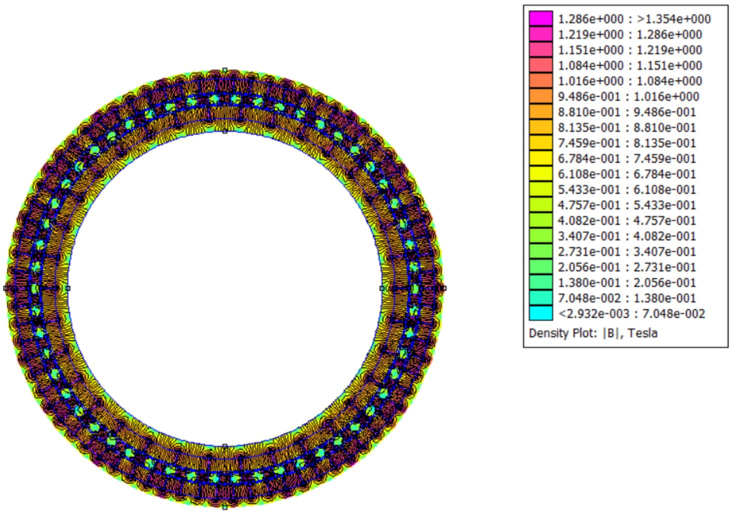

Figure 5.22: M-36 steel FEM plot

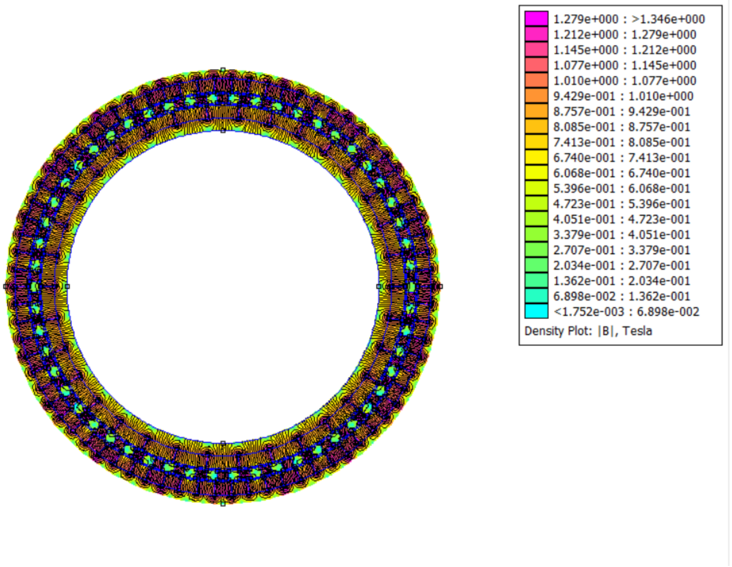

Figure 5.23: Carpenter Silicon Core Iron FEM plot

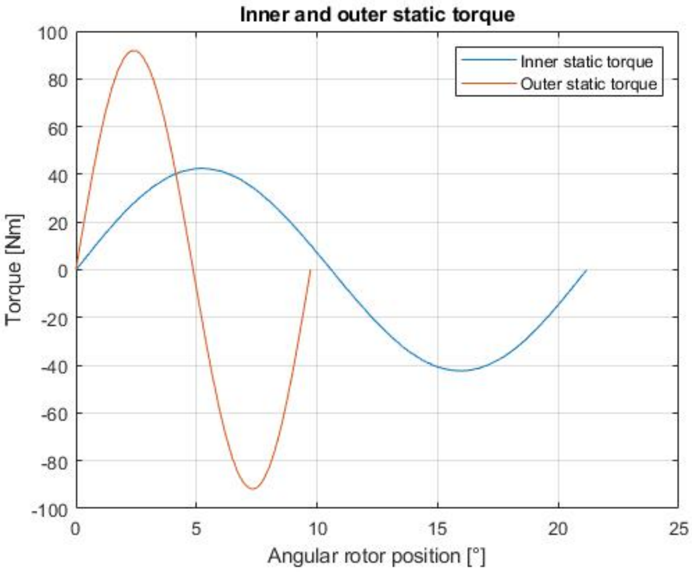

Figure 5.24: Carpenter Silicon Core Iron static torque

5.7 Halbach architecture

Another possible CMG PMs arrangement is the Halbach array. The idea is to create a quasi sinusoidal magnetic flux distribution. Discrete PM segments can realise Halbach PM arrays. Using discrete PM segments in specific directions, applying the superposition method, the PM magnetic induction is reinforced while on the other hand there is a harmonic suppression [14].
In particular, the field is doubled where the flux is confined and the parasitic field effect decreases. The simplest configurations to use this array is the single Halbach field magnet array. But for the CMG application, the dual Halbach field magnet array is applied [15].

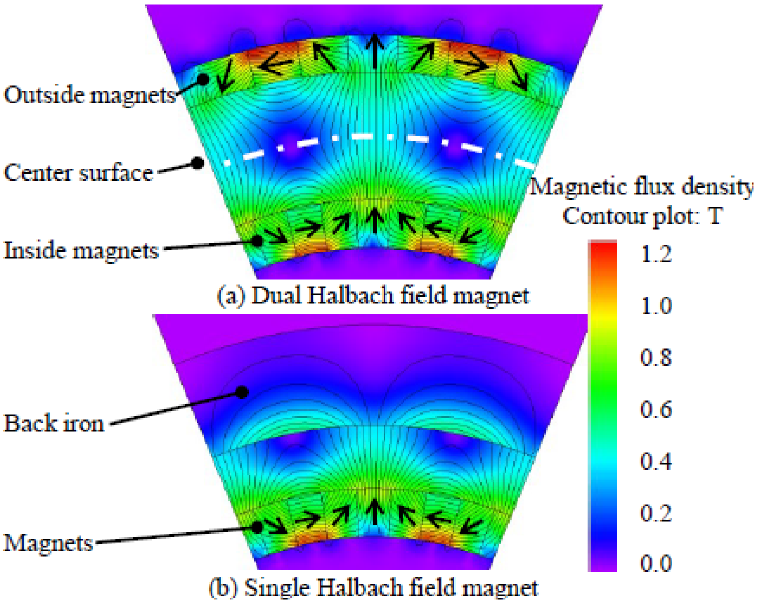

Figure 5.25: Base Halbach definition [15]

The basic array configuration consists of two permament magnets around the pole shifted of 90° . As long as cross section of the PM is square, a strong and sinusoidal magnetic flux density distribution appears on one side of the array, while the faint distribution on the other side. The FEMM model has a different geometrical parameter definition because there is no internal and external yoke. The inner and the outer rotor has only the circular PMs array.

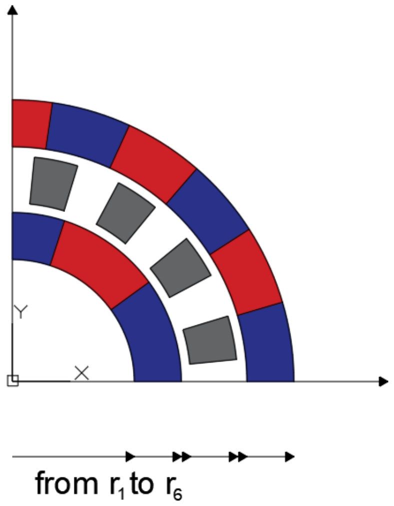

Figure 5.26: Halbach CMG architecture

Geometrical parameter	Value
r_1 to r_6	from the inner to the outer radius
l_{ax}	Axial length: 25 mm
l_{air}	Airgap thickness: 1 mm
$l_{m,in}$	Inner PM thickness
$l_{m,out}$	Outer PM thickness
l_{mod}	Modulator thickness

Table 5.7: Halbach gearbox geometrical definition

5.7.1 First approach

To build the FEMM model, between the poles there are two magnets arranged in quadrature. It means that the permanent magnet portions are characterised by 4 * $(p_{in} + p_{out})$ directions.
To test the torque performances the external radius r_6, the parameter a and the number of the internal and external PM segments ($N_{m,int}$ and $N_{m,ext}$) [15].

$$r_1 = \sqrt{\frac{N_{m,int}^2 - 2(2+a)N_{m,int}\pi + a(2+a)\pi^2}{N_{m,int}^2 + 2(2+a)N_{m,int}\pi + a(2+a)\pi^2}} r_6 \tag{5.10}$$

$$r_2 = \frac{N_{m,int} - a\pi}{\sqrt{N_{m,int}^2 + 2(2+a)N_{m,int}\pi + a(2+a)\pi^2}} r_6 \tag{5.11}$$

$$r_5 = \frac{(N_{m,ext} - a\pi)(N_{m,ext} + a\pi)}{(N_{m,ext} - a\pi)\sqrt{N_{m,ext}^2 + 2(2+a)N_{m,ext}\pi + a(2+a)\pi^2}} r_6 \tag{5.12}$$

	Topology			
	$p_{in} = 5$ $p_{out} = 11$	$p_{in} = 6$ $p_{out} = 13$	$p_{in} = 11$ $p_{out} = 23$	$p_{in} = 17$ $p_{out} = 37$
r_5	88.21 mm	89.75 mm	94 mm	96 mm
r_4	87.20 mm	88.75 mm	93 mm	95 mm
r_3	79.16 mm	81.83 mm	80.9mm	92.79 mm
r_2	78.16 mm	80.83 mm	79.9 mm	91.79 mm
r_1	47.54 mm	55.72 mm	66.14 mm	82.87 mm
$l_{m,in}$	30.62 mm	25.11 mm	13.76 mm	8.92 mm
$l_{m,out}$	11.79 mm	10.25 mm	6 mm	4 mm
l_{mod}	8.04 mm	6.92 mm	3.72 mm	2.21 mm
m	4.04 kg	3.57 mm	2.25 kg	1.53 kg

Table 5.8: Geometrical parameters FEMM model for $r_6 = 100$ mm

The difference $r_5 - r_2$ is the sum $2l_{air} + l_{mod}$. To know the modulator thickness, the air gap thickness is assumed to be 1 mm. From this plot models if p_{in} is small, the PM thickness has a big impact on the geometry definition, and the external field does not hit the modulator. To give a real field lines distribution a small air layer of thickness 3 mm was done in the internal and the external part of the gearbox.

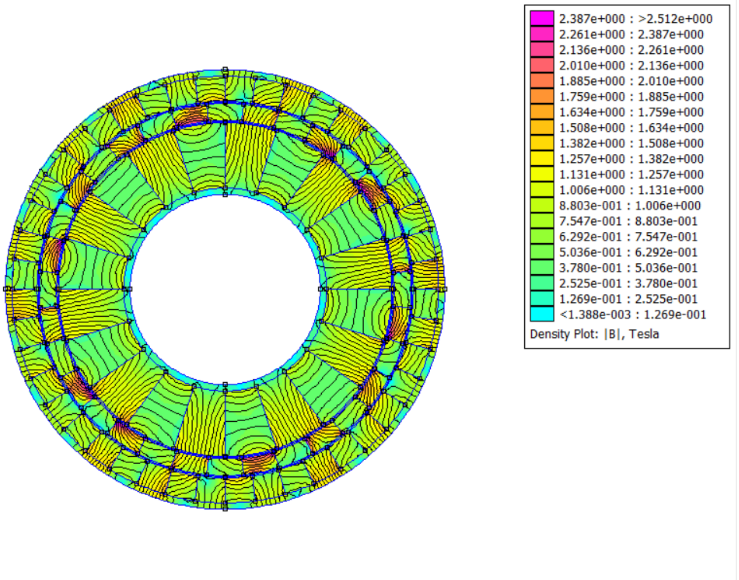

Figure 5.27: FEMM plot with $p_{in} = 5$

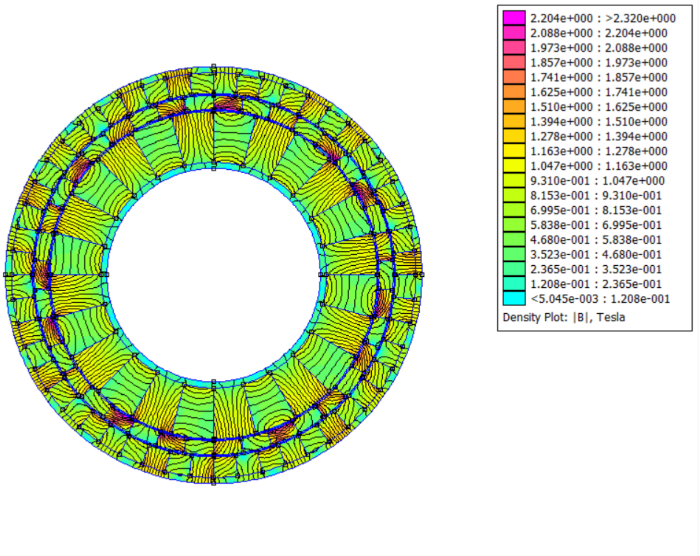

Figure 5.28: FEMM plot with $p_{in} = 6$

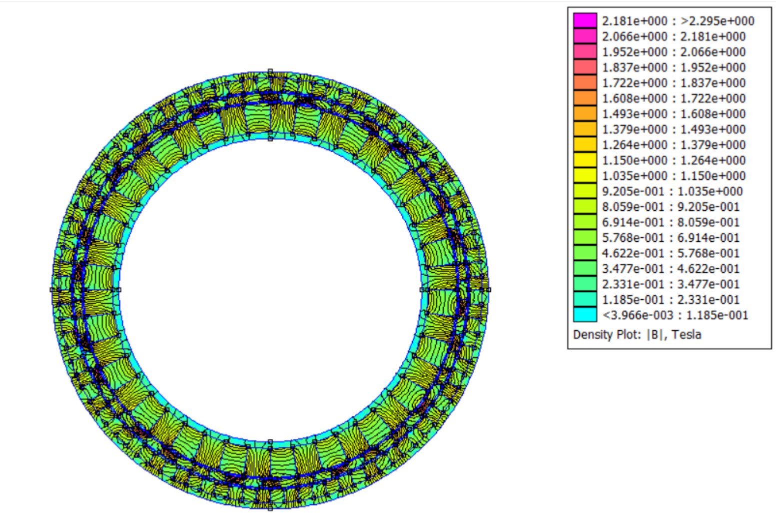

Figure 5.29: FEMM plot with $p_{in} = 11$

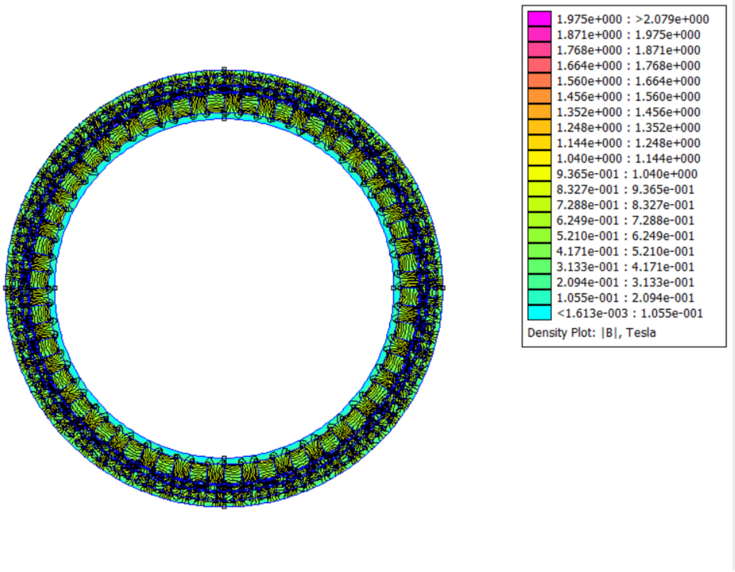

Figure 5.30: FEMM plot with $p_{in} = 17$

The torque has a reduced width and this means that with the mechanical inertia, the two rotors doesn't work well. Moreover, if the pair of poles number increases, the ripple response is caused by numerical errors.

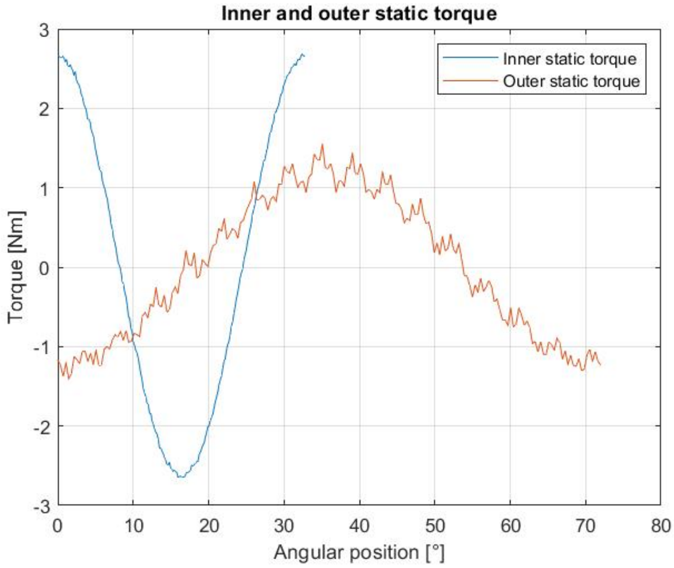

Figure 5.31: Static torque characteristic with $p_{in} = 5$

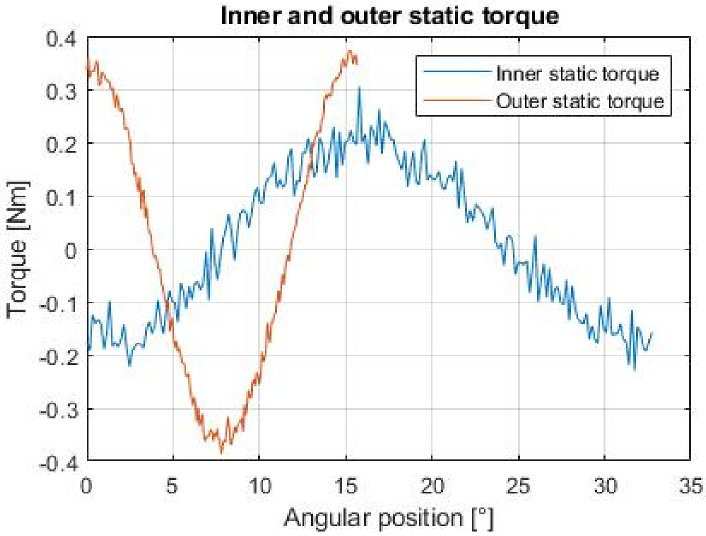

Figure 5.32: Static torque characteristic with $p_{in} = 11$

5.7.2 Second approach

This approach is simple than the first. It is interesting to see the CMG impact in the case of constant mass. The prototype analysed has the same thickness for the inner and the outer PM, and the modulator thickness.

Geometrical parameter	Value
r_1	80 mm
r_2	86 mm
r_3	87 mm
r_4	93 mm
r_5	94 mm
r_6	100 mm
l_{ax}	Axial length: 25 mm
l_{air}	Airgap thickness: 1 mm
$l_{m,in}$	Inner PM thickness: 6 mm
$l_{m,out}$	Outer PM thickness: 6 mm
l_{mod}	Modulator thickness: 6 mm
Mass	2.28 kg
Useful volume	$3.68 * 10^{-4}$ m^3

Table 5.9: Geometrical definition for the second Halbach approach

To reduce the mass proportion two different models were used. The first model had an inner and an outer air layer, while the second was imagined with two yoke of 3 mm thick. In the first model less field lines pass the modulator to product useful torque. In particular, the magnetic induction in the internal and external layer. In the second model, instead, some field lines passes the modulator and they contributes to a useful torque production like it can be seen in the tables 5.10 and 5.11.

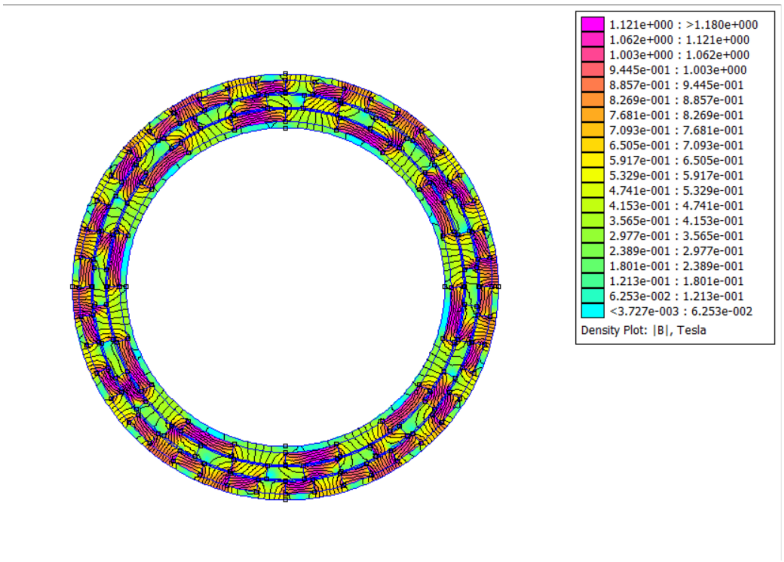

Figure 5.33: FEMM plot without yoke and $p_{in} = 5$

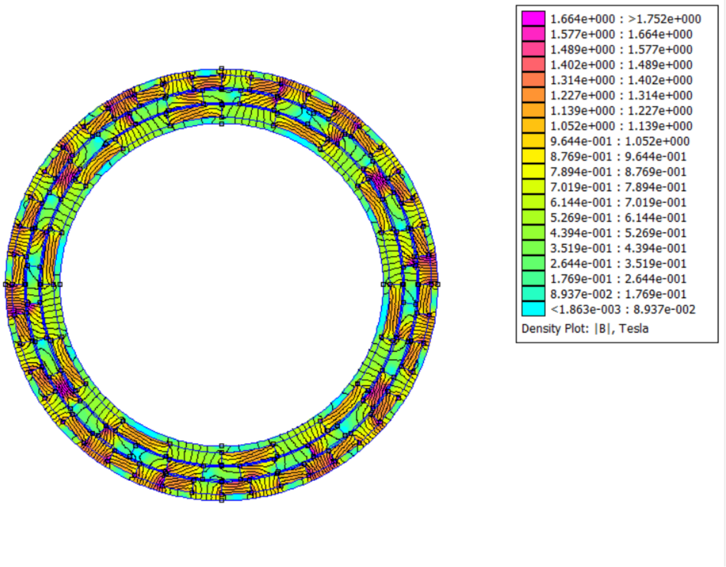

Figure 5.34: FEMM plot with iron yokes and $p_{in} = 5$

	$p_{in} = 5$ $p_{out} = 11$	$p_{in} = 6$ $p_{out} = 13$	$p_{in} = 11$ $p_{out} = 23$	$p_{in} = 17$ $p_{out} = 37$
T_{in}	8.16 Nm	7.06 Nm	3.42 Nm	1.63 Nm
T_{out}	15.93 Nm	14.89 Nm	6.98 Nm	0.94 Nm
Inner vol torque	22.2 kNm/m^3	19.2 kNm/m^3	9.3 kNm/m^3	4.43 kNm/m^3
Outer vol torque	43.34 kNm/m^3	40.51 kNm/m^3	18.99 kNm/m^3	2.56 kNm/m^3

Table 5.10: Torque performances without iron yokes

	$p_{in} = 5$ $p_{out} = 11$	$p_{in} = 6$ $p_{out} = 13$	$p_{in} = 11$ $p_{out} = 23$	$p_{in} = 17$ $p_{out} = 37$
T_{in}	16.75 Nm	17.08 Nm	14.72 Nm	6.55 Nm
T_{out}	34.76 Nm	36.55 Nm	30.55Nm	13.79 Nm
Inner vol torque	45.57 kNm/m^3	46.47 kNm/m^3	40.05 kNm/m^3	17.89 kNm/m^3
Outer vol torque	94.57 kNm/m^3	99.44 kNm/m^3	83.11 kNm/m^3	37.52 kNm/m^3

Table 5.11: Torque performances with the iron yokes

As the tables and figures confirm, the static torque characteristic peaks and the volumetric torque density is near to 100 kNm/m^3.

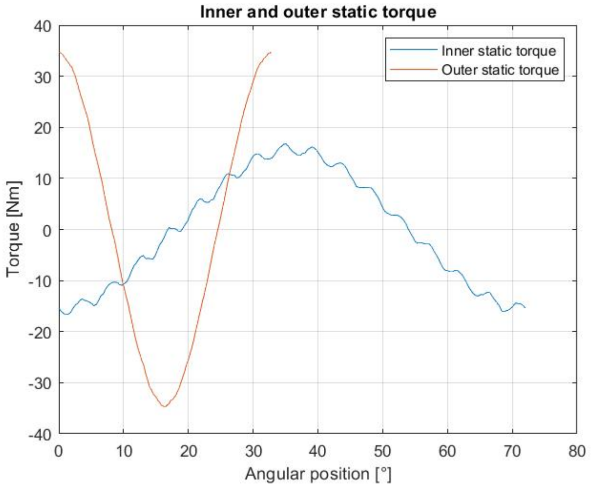

Figure 5.35: Static torque with the iron yoke and $p_{in} = 5$

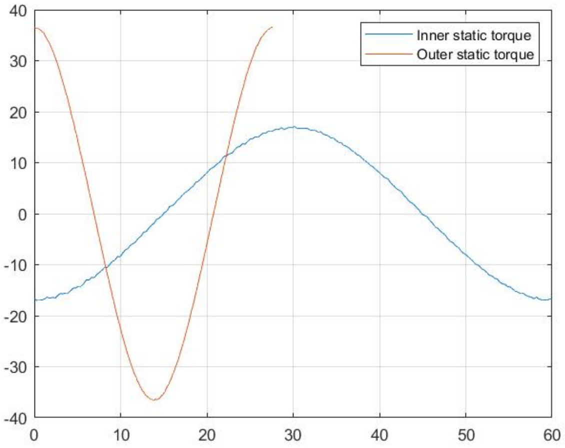

Figure 5.36: Static torque with the iron yoke and $p_{in} = 6$

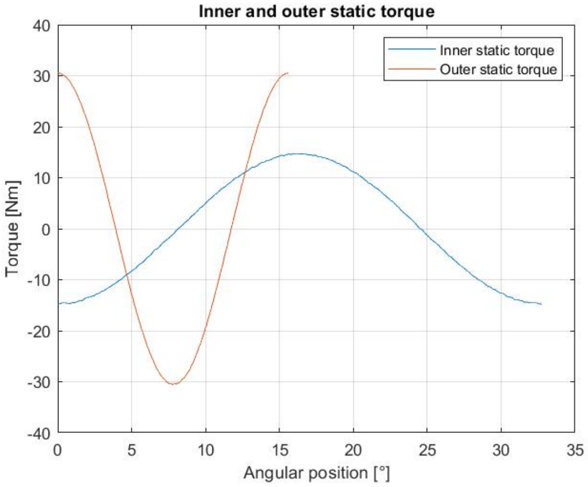

Figure 5.37: Static torque with the iron yoke and $p_{in} = 11$

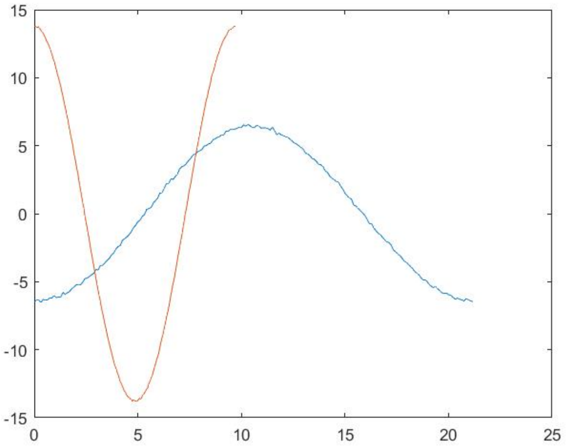

Figure 5.38: Static torque with the iron yoke and $p_{in} = 17$

Chapter 6

Conclusion

In this work, the coaxial magnetic gearbox represents a valid alternative to mechanical turns in many domains. The existing model developed neglects some effects material's real properties because with the first approach used in the simulations, materials are considered linear. The FEMM model provides a first torque performances approach but does not consider the real material behaviour.

A sizing approach was chosen, focusing on the ferromagnetic material specifications and obtaining the maximum torque. The analysis started for the oil pump gives an agreement with the volumetric torque developed using a mechanical gear ($100 - 150$ kNm/m^3). Concerning the mass, there are big differences because the mechanical gear weight is inside the order of kgs. Moreover, referring to the band diameter in the CMG context, the mass is more important, and the other accessories equipment are excluded.

A parametric analysis was carried out to understand the best way to utilize ferromagnetic materials. This analysis shows that with an outer radius CMG increase, the volumes are better exploited and then it gives better performances. This thesis is confirmed considering that with the maximum outer radius $r_8 =$ 200 mm, the volumetric torque gives a linear curve as p_{in} increases. Furthermore, there are no relevant differences comparing performances between two non-linear Fe-Si materials and a linear ferromagnetic material with relative magnetic permeability $\mu_r = 1000$.

Trying to reduce CMG mass, the Halbach configuration was proposed with and without ferromagnetic yokes. In the configuration without external yokes, the torque performance is significantly reduced. In contrast, with the iron yokes use, performances in terms of peak static torque increases as the pole pairs p_{in} and p_{out} decrease. The next step will be to optimize the Halbach architecture to obtain better performances.

The maximum inner volumetric torque is 120 kNm/m^3, referring to the classic mechanical gear. On the other hand, using the Halbach array, the highest volumetric torque is 94.6 kNm/m^3 for the structure with the support yokes, and 43.4 kNm/m^3 for the structure without support yokes.

The simulation time depends on the CMG model geometry. With $p_{in} = 5$ the mesh has 55000 elements against 160000 elements for $p_{in} = 17$. Moving on to more complex geometries, the finite element simulation time doubles from 1.5 h to about 3 hours. In addition, the non-linearity leads to further delays.

Finally, to highlight the torque characteristic ripples, it was chosen to collect 200 points obtaining a good function resolution.

Appendix A

MG building code

```
%% MG design file
load('MG_geom');
openfemm
newdocument(0)
%% Material definition
% Air definition
mi_addmaterial('Air',1,1,0,0);
% Iron definition
mi_addmaterial('Iron',1000,1000,0,0);
%Permanent magnet definition with B_r = 1.2 [T]
mi_getmaterial('N35');
%% Building outer PMs
angleout=2*pi/Nm(2);
angleoutd=360/Nm(2);
mi_addnode(r(6),0);
mi_addnode(r(5),0);
% Creation node outer PM
for i=1:Nm(2)
mi_addnode(r(6)*cos(i*angleout),r(6)*sin(i*angleout));
mi_addnode(r(5)*cos(i*angleout),r(5)*sin(i*angleout));
end
%Creation arc segment outer PM
for i=1:Nm(2)
    mi_addarc(r(6)*cos((i-1)*angleout),r(6)*sin((i-1)*angleout),r(6)*cos(i*angleout),r(6)*sin(i*angleout),angleoutd,1);
    mi_addarc(r(5)*cos((i-1)*angleout),r(5)*sin((i-1)*angleout),r(5)*cos(i*angleout),r(5)*sin(i*angleout),angleoutd,1);
end
% Separation between the different outer poles
mi_addsegment(r(6),0,r(5),0);
for i=1:Nm(2)
```

```
    mi_addsegment(r(6)*cos(i*angleout),r(6)*sin(i*angleout),r(5)*cos(i*angleout),r(5)*sin(i*angleout));
end
%% Building modulator zone
Q=p_in+p_out;
anglem=pi/Q;
anglemd=180/Q;
mi_addnode(r(4)*cos(anglem/2),r(4)*sin(anglem/2));
mi_addnode(r(3)*cos(anglem/2),r(3)*sin(anglem/2));
thetam=3/2*anglem;
for i=1:2*Q-1
    mi_addnode(r(4)*cos(thetam),r(4)*sin(thetam));
    mi_addnode(r(3)*cos(thetam),r(3)*sin(thetam));
    thetam=thetam+anglem;
end
% Modulator segments
for i=1:2*Q
    mi_addnode(r(4)*cos(thetam),r(4)*sin(thetam));
    mi_addnode(r(3)*cos(thetam),r(3)*sin(thetam));
    mi_addsegment(r(4)*cos(thetam),r(4)*sin(thetam),r(3)*cos(thetam),r(3)*sin(thetam));
    thetam=thetam+anglem;
end
thetam=anglem/2;
for i=1:Q
    mi_addarc(r(4)*cos(thetam),r(4)*sin(thetam),r(4)*cos(thetam+anglem),r(4)*sin(thetam+anglem),anglemd,1);
    mi_addarc(r(3)*cos(thetam),r(3)*sin(thetam),r(3)*cos(thetam+anglem),r(3)*sin(thetam+anglem),anglemd,1);
    thetam=thetam+2*anglem;
end
%% Building inner PMs
anglein=2*pi/Nm(1);
angleind=360/Nm(1);
mi_addnode(r(2),0);
mi_addnode(r(1),0);
% Creation nodes inner PMs
for i=1:Nm(1)
mi_addnode(r(2)*cos(i*anglein),r(2)*sin(i*anglein));
mi_addnode(r(1)*cos(i*anglein),r(1)*sin(i*anglein));
end
%Creation arc segments inner PMs
for i=1:Nm(1)
     mi_addarc(r(2)*cos((i-1)*anglein),r(2)*sin((i-1)*anglein),r(2)*cos(i*anglein),r(2)*sin(i*anglein),angleind,1);
     mi_addarc(r(1)*cos((i-1)*anglein),r(1)*sin((i-1)*anglein),r(1)*cos(i*anglein),r(1)*sin(i*anglein),angleind,1);
end
% Separation between differents inner poles
```

```
mi_addsegment(r(2),0,r(1),0);
for i=1:Nm(1)
    mi_addsegment(r(2)*cos(i*anglein),r(2)*sin(i*anglein),r(1)*cos(i*anglein),r(1)*sin(i*anglein));
end
%% Add block label for each constitutive layer
% Inner cylinder zone
mi_addblocklabel(0,0);
mi_selectlabel(0,0);
mi_setblockprop('<No Mesh>',1,0,'',0,0,0);
mi_selectlabel(0,0);
% Inner PM layer definition
in=anglein/2;
for i=1:2*p_in
    ind=180/pi*in;
    if mod(i,2) == 1
            mi_addblocklabel((r(1)+r(2))/2*cos(in),(r(1)+r(2))/2*sin(in));
            mi_selectlabel((r(1)+r(2))/2*cos(in),(r(1)+r(2))/2*sin(in));
            mi_setblockprop('N35',1,0,0,ind,0,0);
            mi_selectlabel((r(1)+r(2))/2*cos(in),(r(1)+r(2))/2*sin(in));
            in=in+anglein;
            ind=180/pi*in;
            mi_addblocklabel((r(1)+r(2))/2*cos(in),(r(1)+r(2))/2*sin(in));
            mi_selectlabel((r(1)+r(2))/2*cos(in),(r(1)+r(2))/2*sin(in));
            mi_setblockprop('N35',1,0,0,ind-90,0,0);
            mi_selectlabel((r(1)+r(2))/2*cos(in),(r(1)+r(2))/2*sin(in));
    else
            mi_addblocklabel((r(1)+r(2))/2*cos(in),(r(1)+r(2))/2*sin(in));
            mi_selectlabel((r(1)+r(2))/2*cos(in),(r(1)+r(2))/2*sin(in));
            mi_setblockprop('N35',1,0,0,ind+180,0,0);
            mi_selectlabel((r(1)+r(2))/2*cos(in),(r(1)+r(2))/2*sin(in));
            in=in+anglein;
            ind=180/pi*in;
            mi_addblocklabel((r(1)+r(2))/2*cos(in),(r(1)+r(2))/2*sin(in));
            mi_selectlabel((r(1)+r(2))/2*cos(in),(r(1)+r(2))/2*sin(in));
            mi_setblockprop('N35',1,0,0,ind+90,0,0);
            mi_selectlabel((r(1)+r(2))/2*cos(in),(r(1)+r(2))/2*sin(in));
```

```
    end
    in=in+anglein;
end
% Airgap layer definition
mi_addnode(r(2)+0.5,0);
mi_addnode(0,r(2)+0.5);
mi_addnode(-(r(2)+0.5),0);
mi_addnode(0,-(r(2)+0.5));
mi_addarc(r(2)+0.5,0,0,r(2)+0.5,90,1);
mi_addarc(0,r(2)+0.5,-(r(2)+0.5),0,90,1);
mi_addarc(-(r(2)+0.5),0,0,-(r(2)+0.5),90,1);
mi_addarc(0,-(r(2)+0.5),r(2)+0.5,0,90,1);
mi_addblocklabel(r(2)+0.25,0);
mi_selectlabel(r(2)+0.25,0);
mi_setblockprop('Air',1,0,0,0,0,0);
mi_addblocklabel(r(2)+0.75,0);
mi_selectlabel(r(2)+0.75,0);
mi_setblockprop('Air',1,0,0,0,0,0);
mi_addnode(r(4)+0.5,0);
mi_addnode(0,r(4)+0.5);
mi_addnode(-(r(4)+0.5),0);
mi_addnode(0,-(r(4)+0.5));
mi_addarc(r(4)+0.5,0,0,r(4)+0.5,90,1);
mi_addarc(0,r(4)+0.5,-(r(4)+0.5),0,90,1);
mi_addarc(-(r(4)+0.5),0,0,-(r(4)+0.5),90,1);
mi_addarc(0,-(r(4)+0.5),r(4)+0.5,0,90,1);
mi_addblocklabel(r(4)+0.25,0);
mi_selectlabel(r(4)+0.25,0);
mi_setblockprop('Air',1,0,0,0,0,0);
mi_addblocklabel(r(4)+0.75,0);
mi_selectlabel(r(4)+0.75,0);
mi_setblockprop('Air',1,0,0,0,0,0);
% Definition modulator air zones
thetainm=0;
for i=1:Q
mi_addarc(r(3)*cos(thetainm-anglem/2),r(3)*sin(thetainm-anglem/2),r(3)*cos(thetainm+anglem/2),r(3)*sin(thetainm+anglem/2),anglemd,1);
mi_addarc(r(4)*cos(thetainm-anglem/2),r(4)*sin(thetainm-anglem/2),r(4)*cos(thetainm+anglem/2),r(4)*sin(thetainm+anglem/2),anglemd,1);
mi_addblocklabel((r(3)+r(4))/2*cos(thetainm),(r(3)+r(4))/2*sin(thetainm));
mi_selectlabel((r(3)+r(4))/2*cos(thetainm),(r(3)+r(4))/2*sin(thetainm));
mi_setblockprop('Air',1,0,0,0,0,0);
mi_selectlabel((r(3)+r(4))/2*cos(thetainm),(r(3)+r(4))/2*sin(thetainm));
thetainm=thetainm+2*anglem;
end
% Modulator definition
```

```
modul=anglem;
for i=1:Q
    mi_addblocklabel((r(3)+r(4))/2*cos(modul),(r(3)+r(4))/2*sin(modul));
    mi_selectlabel((r(3)+r(4))/2*cos(modul),(r(3)+r(4))/2*sin(modul));
    modul=modul+2*anglem;
end
mi_setblockprop('Iron',1,0,0,0,0,0);
modul=anglem;
for i=1:Q
    mi_selectlabel((r(3)+r(4))/2*cos(modul),(r(3)+r(4))/2*sin(modul));
    modul=modul+2*anglem;
end
mi_setblockprop('Iron',1,0,0,0,0,0);
% Outer PM layer definition
out=angleout/2;
for i=1:2*p_out
    outd=out*180/pi;
    if mod(i,2) == 1
        mi_addblocklabel((r(5)+r(6))/2*cos(out),(r(5)+r(6))/2*sin(out));
        mi_selectlabel((r(5)+r(6))/2*cos(out),(r(5)+r(6))/2*sin(out));
        mi_setblockprop('N35',1,0,0,outd,0,0);
        mi_selectlabel((r(5)+r(6))/2*cos(out),(r(5)+r(6))/2*sin(out));
        out=out+angleout;
        outd=180/pi*out;
        mi_addblocklabel((r(5)+r(6))/2*cos(out),(r(5)+r(6))/2*sin(out));
        mi_selectlabel((r(5)+r(6))/2*cos(out),(r(5)+r(6))/2*sin(out));
        mi_setblockprop('N35',1,0,0,outd-90,0,0);
        mi_selectlabel((r(5)+r(6))/2*cos(out),(r(5)+r(6))/2*sin(out));
    else
        mi_addblocklabel((r(5)+r(6))/2*cos(out),(r(5)+r(6))/2*sin(out));
        mi_selectlabel((r(5)+r(6))/2*cos(out),(r(5)+r(6))/2*sin(out));
        mi_setblockprop('N35',1,0,0,outd+180,0,0);
        mi_selectlabel((r(5)+r(6))/2*cos(out),(r(5)+r(6))/2*sin(out));
        out=out+angleout;
        outd=180/pi*out;
        mi_addblocklabel((r(5)+r(6))/2*cos(out),(r(5)+r(6))/2*sin(out));
```

```
        mi_selectlabel((r(5)+r(6))/2*cos(out),(r(5)+r(6))/2*sin(out));
        mi_setblockprop('N35',1,0,0,outd+90,0,0);
        mi_selectlabel((r(5)+r(6))/2*cos(out),(r(5)+r(6))/2*sin(out));
    end
    out=out+angleout;
end
%% Confinate the MG system
% Outer air part layer
mi_addnode(r(6)+3,0);
mi_addnode(0,r(6)+3);
mi_addnode(-(r(6)+3),0);
mi_addnode(0,-(r(6)+3));
mi_addarc(r(6)+3,0,0,r(6)+3,90,1);
mi_addarc(0,r(6)+3,-(r(6)+3),0,90,1);
mi_addarc(-(r(6)+3),0,0,-(r(6)+3),90,1);
mi_addarc(0,-(r(6)+3),r(6)+3,0,90,1);
mi_addblocklabel(r(6)+1.5,0);
mi_selectlabel(r(6)+1.5,0);
mi_setblockprop('Air',1,0,0,0,0,0);
mi_selectlabel(r(6)+1.5,0);
% Inner air part layer
mi_addnode(r(1)-3,0);
mi_addnode(0,r(1)-3);
mi_addnode(-(r(1)-3),0);
mi_addnode(0,-(r(1)-3));
mi_addarc(r(1)-3,0,0,r(1)-3,90,1);
mi_addarc(0,r(1)-3,-(r(1)-3),0,90,1);
mi_addarc(-(r(1)-3),0,0,-(r(1)-3),90,1);
mi_addarc(0,-(r(1)-3),r(1)-3,0,90,1);
mi_addblocklabel(r(1)-1.5,0);
mi_selectlabel(r(1)-1.5,0);
mi_setblockprop('Air',1,0,0,0,0,0);
mi_selectlabel(r(1)-1.5,0);
% Problem definition
mi_probdef(0,'millimeters','planar',1E-8,l_ax,30,0);
%% Save and close the FEMM Magnetic Gearbox system
mi_saveas('MG_accessories_air.fem');
closefemm;
```

Appendix B

Inner static torque characteristic

```
openfemm;
opendocument('MG_accessories_air.fem');
%% Create the inner torque group to rotate and evaluate each rotor configuration
% Select all the inner rotor element
load('MG_geom');
theta_in=0:90/p_in:360-45/p_in;
% Modify the inner segment group
for i=1:size(theta_in,2)
mi_selectsegment((r(1)+r(2))/2*cosd(theta_in(i)),(r(1)+r(2))/2*sind(theta_in(i)));
end
mi_setgroup(1);
% Modify the internal arc of the inner PM
theta_in=45/p_in:90/p_in:360-45/p_in;
for i=1:size(theta_in,2)
    mi_selectarcsegment(r(1)*cosd(theta_in(i)),r(1)*sind(theta_in(i)));
    mi_selectarcsegment(r(2)*cosd(theta_in(i)),r(2)*sind(theta_in(i)));
end
mi_setgroup(1);

% Modify the inner PM label
for i=1:size(theta_in,2)
    mi_selectlabel((r(1)+r(2))/2*cosd(theta_in(i)),(r(1)+r(2))/2*sind(theta_in(i)));
    mi_setgroup(1);
```

```
end
% Know the inner and the outer static torque for each angular position
step=360/(199*p_in);
theta_in=0:360/(199*p_in):360/p_in;
T_in=zeros(2,size(theta_in,2));
for i=1:size(theta_in,2)
    mi_createmesh;
    mi_analyse;
    mi_loadsolution;
    mo_selectpoint((r(2)+r(3))/2,0);
    mo_selectpoint(0,(r(2)+r(3))/2);
    mo_selectpoint(-(r(2)+r(3))/2,0);
    mo_selectpoint(0,-(r(2)+r(3))/2);
    mo_selectpoint((r(2)+r(3))/2,0);
    T_in(:,i)=mo_lineintegral(4);
    mi_selectgroup(1);
    mi_moverotate(0,0,step);
    fprintf('Iteration: %d \n',i);
end
save('Inner_static_torque','theta_in','T_in');
closefemm;
```

Appendix C

Outer static torque characteristics

```
close all;
clear all;
clc;
openfemm;
opendocument('MG_accessories_air.fem');
%% Create the outer torque group to rotate and evaluate each rotor configuration
% Select all the outer rotor elements
load('MG_geom');
theta_out=0:90/p_out:360-45/p_out;
% Modify the inner segment group
for i=1:size(theta_out,2)
mi_selectsegment((r(5)+r(6))/2*cosd(theta_out(i)),(r(5)+r(6))/2*sind(theta_out(i)));
end
mi_setgroup(2);
% Modify the external arc of the outer PM
theta_out=45/p_out:90/p_out:360-45/p_out;
for i=1:size(theta_out,2)
    mi_selectarcsegment(r(5)*cosd(theta_out(i)),r(5)*sind(theta_out(i)));
    mi_selectarcsegment(r(6)*cosd(theta_out(i)),r(6)*sind(theta_out(i)));
end
mi_setgroup(2);
% Modify the outer PM label
for i=1:size(theta_out,2)
```

```
    mi_selectlabel((r(5)+r(6))/2*cosd(theta_out(i)),(r(5)+r(6))/2*sind(theta_out(i)));
    mi_setgroup(2);
end
% Know the outer static torque for each angular position
step=360/(199*p_out);
theta_out=0:step:360/p_out;
T_out=zeros(2,size(theta_out,2));
for i=1:size(theta_out,2)
    mi_createmesh;
    mi_analyse;
    mi_loadsolution;
    mo_selectpoint((r(4)+r(5))/2,0);
    mo_selectpoint(0,(r(4)+r(5))/2);
    mo_selectpoint(-(r(4)+r(5))/2,0);
    mo_selectpoint(0,-(r(4)+r(5))/2);
    mo_selectpoint((r(4)+r(5))/2,0);
    T_out(:,i)=mo_lineintegral(4);
    mi_selectgroup(2);
    mi_moverotate(0,0,-step);
    fprintf('Iteration: %d \n',i);
end
save('Outer_static_torque','theta_out','T_out');
closefemm;
```

Bibliography

[1] Thierry Lubin, Smail Mezani, and Abderrezak Rezzoug. «Analytical Computation of the Magnetic Field Distribution in a Magnetic Gear». eng. In: *IEEE transactions on magnetics* 46.7 (2010), pp. 2611–2621. ISSN: 0018-9464 (cit. on pp. 2–4, 7, 13, 17).

[2] Sallehuddin Mohamed Haris Abdullah Al Faysal*. *Development of Magnetic Gears: A Review*. 2018. URL: `https://doi.org/10.17576/jkukm-2018-si1(7)-06` (cit. on p. 2).

[3] K Atallah and D Howe. «A novel high-performance magnetic gear». eng. In: *IEEE transactions on magnetics* 37.4 (2001), pp. 2844–2846. ISSN: 0018-9464 (cit. on p. 2).

[4] Libing Jing, Jun Gong, and Tong Ben. «Analytical Method for Magnetic Field of Eccentric Magnetic Harmonic Gear». eng. In: *IEEE access* 8 (2020), pp. 34236–34245. ISSN: 2169-3536 (cit. on pp. 3, 4).

[5] M Okano, K Tsurumoto, S Togo, N Tamada, and S Fuchino. «Characteristics of the magnetic gear using a bulk high-Tc superconductor». eng. In: *IEEE transactions on applied superconductivity* 12.1 (2002), pp. 979–983. ISSN: 1051-8223 (cit. on p. 3).

[6] Cheng-Chi Huang, Mi-Ching Tsai, D.G Dorrell, and Bor-Jeng Lin. «Development of a Magnetic Planetary Gearbox». eng. In: *IEEE transactions on magnetics* 44.3 (2008), pp. 403–412. ISSN: 0018-9464. DOI: `10.1109/TMAG.2007.914665` (cit. on pp. 5, 6).

[7] A. F. F. Filho C. G. C. Neves. *Magnetic Gearing Electromagnetic Concepts*. 2019. URL: `http://www.scielo.br/scielo.php?script=sci_arttext&pid=S2179-10742017000100108&lng=en&tlng=en` (cit. on p. 8).

[8] Chao Wang Xiaoxu Zhang * Xiao Liu and Zhe Chen. *Analysis and Design Optimization of a Coaxial Surface-Mounted Permanent-Magnet Magnetic Gear*. 2014. URL: `https://doi.org/10.3390/en7128535` (cit. on pp. 9, 10, 15, 17, 19).

[9] Carlos G. C Neves, Diogo Luciano Figueiredo, Ály Ferreira Flores, and Anderson Santos Nunes. «Magnetic gear: A review». eng. In: *2014 11th IEEE/IAS International Conference on Industry Applications*. IEEE, 2014, pp. 1–6. ISBN: 9781479955503 (cit. on p. 12).

[10] Melaine Desvaux, Benjamin Traulle, Roman Le Goff Latimier, Stephane Sire, Bernard Multon, and Hamid Ben Ahmed. «Computation Time Analysis of the Magnetic Gear Analytical Model». eng. In: *IEEE transactions on magnetics* 53.5 (2017), pp. 1–9. ISSN: 0018-9464 (cit. on p. 14).

[11] Linni Jian, Zhengxing Deng, Yujun Shi, Jin Wei, and C. C Chan. «The Mechanism How Coaxial Magnetic Gear Transmits Magnetic Torques Between Its Two Rotors: Detailed Analysis of Torque Distribution on Modulating Ring». eng. In: *IEEE/ASME transactions on mechatronics* 24.2 (2019), pp. 763–773. ISSN: 1083-4435 (cit. on p. 19).

[12] Vincenzo Cirimele, Luca Dimauro, Maurizio Repetto, and Elvio Bonisoli. «Multi-objective optimisation of a magnetic gear for powertrain applications». eng. In: (2019) (cit. on p. 21).

[13] Debarupa Som, Kang Li, Joshua Kadel, Jason Wright, Sina Modaresahmadi, Jonathan Z Bird, and W William. «Analysis and Testing of a Coaxial Magnetic Gearbox With Flux Concentration Halbach Rotors». eng. In: *IEEE transactions on magnetics* 53.11 (2017), pp. 1–6. ISSN: 0018-9464 (cit. on p. 27).

[14] Linni Jian and K T Chau. «A Coaxial Magnetic Gear With Halbach Permanent-Magnet Arrays». eng. In: *IEEE transactions on energy conversion* 25.2 (2010), pp. 319–328. ISSN: 0885-8969 (cit. on p. 41).

[15] N. Morimura, H. Suzuki, and M. Morishita. «Single Halbach Field Magnet Desined from Dual Halbach Field Magnet for Rotating Machines». In: *2018 21st International Conference on Electrical Machines and Systems (ICEMS)*. 2018, pp. 27–30. DOI: `10.23919/ICEMS.2018.8549280` (cit. on pp. 41, 43).